$Al_{11}Mn_4$ formation on Al_8Mn_5 during the solidification and heat treatment of AZ-series magnesium alloys

J.W. Xian[1,*], L. Peng[1], G. Zeng[2], D. Wang[1], C.M. Gourlay[1,*]

[1] Department of Materials, Imperial College London, London. SW7 2AZ. UK

[2] School of Materials Science and Engineering, Central South University, Changsha, 410083, China

* Corresponding author j.xian@imperial.ac.uk; c.gourlay@imperial.ac.uk

Abstract

The crystallography and kinetics of $Al_{11}Mn_4$ formation on Al_8Mn_5 have been studied in magnesium alloys AZ80 / AZ91 and AZ31. During solidification, $Al_{11}Mn_4$ formation was promoted by low cooling rates where triclinic $Al_{11}Mn_4$ nucleated on rhombohedral Al_8Mn_5 particles with one of multiple related orientation relationships (ORs) and their variants. $Al_{11}Mn_4$ grew as (010) plates that were commonly twinned and the interrelationships among $Al_{11}Mn_4$ twins, Al_8Mn_5 twins and Al_8Mn_5-$Al_{11}Mn_4$ ORs are discussed. During solid state heat treatment at 410 °C, Al_8Mn_5 particles transformed into $Al_{11}Mn_4$ by a core-shell reaction with cracking in the $Al_{11}Mn_4$ shell. The solid-state reaction kinetics were consistent with interface reaction controlled growth. The results show that heat treatment can be used to tailor the Al-Mn compound in contact with the matrix (Mg) phase which may enable some control of corrosion performance.

Keywords: electron backscatter diffraction; crystallography; orientation relationship; magnesium alloys; intermetallics

1. Introduction

AZ-series alloys are among the most widely used structural magnesium alloys. Compositions close to Mg-9Al-0.7Zn-0.2Mn (wt%) lie within the composition ranges of various high purity ASTM alloy specifications including the wrought alloy AZ80A [1], the sand casting alloy AZ91E [2], and the high pressure die casting (HPDC) alloy AZ91D [3], and are also within the composition range of AZ91 powders for additive manufacturing [4]. Compositions close to Mg-3Al-1Zn-0.5Mn (wt%) are used as the wrought alloy AZ31B. After casting, AZ80/AZ91 and AZ31 usually contain equiaxed dendritic α-Mg grains [5], a network of $Mg_{17}Al_{12}$ [6–9] that forms by a non-equilibrium eutectic reaction, and a small volume fraction of Al-Mn intermetallic compounds (IMCs), with Al_8Mn_5 being the majority Al-Mn IMC. These manganese aluminides occupy only ~0.25 % of the volume and are relatively small (typically 100nm - 1μm in HPDC [8,10,11] and 4-15 μm at sand casting cooling rates [9]), yet they play an important role in corrosion performance [12–15].

A body of past research has investigated the dissolution of non-equilibrium eutectic $Mg_{17}Al_{12}$ during solution heat treatment [16–20], and its effect on corrosion [21–23], as well as the crystallography and kinetics of $Mg_{17}Al_{12}$ precipitation [24–27]. However, little work has examined how heat treatment alters the Al-Mn IMCs present in AZ91 / AZ80 [28]. It is common in past papers to state that Al_8Mn_5 is stable (does not transform) during solution heat treatment of AZ80/AZ91, e.g.[17,29,30]. Yet, calculations in commercial thermodynamics packages Thermo-Calc [31] and Pandat [32] suggest there is a driving force for significant changes in the Al-Mn IMCs if an alloy that solidified under Scheil conditions is equilibrated at a typical solutionising temperature (400-420 °C).

For example, results from the Thermo-Calc TCMG4.0 database are shown in Fig. 1 using the Mg-Al-Mn ternary system as an approximation for AZ91/AZ80. In the ternary liquidus projection in Fig. 1 (a), the liquid composition path is shown for an alloy with bulk composition Mg-8.95Al-0.19Mn (wt%), coloured by the reaction taking place assuming the Scheil model. Solidification begins with L → Al_8Mn_5 (red) followed by L → α-Mg + Al_8Mn_5 (green), L → α-Mg + $Al_{11}Mn_4$ (purple) and then L → α-Mg + Al_4Mn (yellow) noting that, since the Scheil model assumes no diffusion in the solid phases, the liquid composition jumps over two quasi-peritectic points, indicated by black dots. Finally, the liquid composition reaches a ternary eutectic point and solidification is completed by the reaction L → α-Mg + $Mg_{17}Al_{12}$ + Al_4Mn (orange circle). Fig. 1(b) shows the development of solid phases for Scheil solidification using the same colour scheme as Fig. 1(a). Black dots indicate where a phase stops forming. Note that the different solid phases have very different mass percentages and have been plotted on a logarithmic scale (similar to previous work [33,34]). From Fig. 1(a) and (b), $Al_{11}Mn_4$ is expected to initiate by a quasi-peritectic reaction on the pre-existing Al_8Mn_5 and, later on cooling, Al_4Mn on the $Al_{11}Mn_4$. The final amounts of each phase after Scheil solidification are indicated with vertical black arrows where it can be seen that the mass percentages of Al-Mn intermetallics are 0.23% Al_8Mn_5, 0.008% $Al_{11}Mn_4$ and 0.004% Al_4Mn, according to these calculations. That is to say, ~95% of the total mass fraction of Al-Mn IMCs after Scheil solidification of Mg-8.95Al-0.19Mn is Al_8Mn_5 [35–37]. At the same time, the Scheil model does not consider nucleation or the faceted growth kinetics of these complex IMCs.

Performing similar calculations including additional elements (e.g. 0.7wt% Zn and 0.001wt% Fe) altered the detail but did not affect the key points described above regarding the Al-Mn

compounds. Similarly, the same key conclusions could be drawn when repeating the calculations in Pandat [32]. The solidification of AZ31 differs in the development of the α-Mg and $Mg_{17}Al_{12}$ phases, but the calculated formation of the Al-Mn compounds is similar to AZ80/AZ91.

The calculated isopleth in Fig. 1(c) places the composition Mg-9Al-0.19Mn in the α-Mg + Al_4Mn two phase region at 400-420°C, whereas experiments on the 400°C Mg-Al-Mn isothermal section have indicated that this composition is in the α-Mg + $Al_{11}Mn_4$ two phase region [38] as did the CALPHAD model in [39]. From this, the majority Al_8Mn_5 phase formed during solidification would be expected to transform into $Al_{11}Mn_4$ during solution heat treatment. While many papers mention $Al_{11}Mn_4$ in AM and AZ-series Mg alloys, e.g. [40–43], little is known on $Al_{11}Mn_4$ formation in these alloys during solidification and heat treatment. The transformation to $Al_{11}Mn_4$ during solutionising is potentially interesting from a corrosion perspective since studies have shown that Al-Mn IMCs with higher Al:Mn ratios act as less efficient micro-cathodes in the α-Mg matrix, decreasing the corrosion rate [44,45].

Based on the considerations above, a study was performed to understand the formation of $Al_{11}Mn_4$ during the solidification of Mg-3Al-1Zn-0.5Mn and Mg-9Al-0.7Zn-0.2Mn and the solution heat treatment of Mg-9Al-0.7Zn-0.2Mn, building from our previous work on Al_8Mn_5 solidification [9]. The study was conducted with three main aims: (i) To determine the nucleation and faceted growth crystallography of $Al_{11}Mn_4$ during solidification; (ii) To quantify the solid state transformation kinetics of Al-Mn particles during solution heat treatment at 410 °C; and (iii) To explore the potential of using a solution heat treatment to control the Al-Mn IMCs in AZ91 / AZ80.

2. Methods

Commercial ingots were used with compositions (i) Mg-8.95Al-0.72Zn-0.19Mn-<0.001Fe (wt%) that conforms with ASTM specifications for high purity AZ91D, AZ91E, and AZ80A, and (ii) Mg-3.1Al-1.1Zn-0.5Mn-0.003Fe (wt%) that conforms with AZ31B.

For solidification experiments, cylinders with ∅= 9 mm and height 15 mm were machined from the ingots and placed inside an Al_2O_3 flat-bottomed cylindrical crucible with inner diameter similar to the sample. This was then encapsulated in a quartz tube backfilled with Ar and placed in a furnace at 700 °C. After 120 minutes, the samples were solidified at one of two cooling rates. (i) In the first method, the 700 °C quartz tube was removed from the furnace to the vertical cylindrical hole within a tool steel mould at room temperature; this gave a cooling rate of ~1 $K{\cdot}s^{-1}$. (ii) For slower cooling, the furnace was turned off and lid removed, resulting in a cooling rate of ~0.1 $K{\cdot}s^{-1}$. In this case, some samples were switched to the faster cooling method from 430 °C to minimise transformations during slow solid-state cooling (after solidification).

For solution heat treatment experiments, specimens were cut from similar locations of the original ingot into ~20mm×20mm×20mm cubes. Specimens were held in a forced-air convection oven at 410±4°C for different times (0, 0.5, 1, 2, 3, 5, 6, 21 and 90 days) and then were cooled in water. For heat treatments longer than 6 days, samples were sealed in quartz tubes backfilled with argon. Samples were coated by boron nitride for other shorter time heat treatments.

For microstructural analysis, cross-sections were ground and polished down to a 0.05 μm colloidal silica finish. For EBSD characterisation, an additional step of preparation was Ar-ion milling for 40 min using a Gatan PECSII instrument. The sample rotation rate was 2 rpm, and

a 4 kV accelerated beam and a grazing incidence angle of 4° were used. For the investigation of the three-dimensional morphology and crystallography of intermetallic phases, some samples were etched in a solution of 10% HNO_3 in ethanol for 5-10 min to selectively remove the α-Mg matrix.

A Zeiss AURIGA field emission gun scanning electron microscope (FEG-SEM) with an Oxford Instruments INCA x-sight energy dispersive X-ray spectroscopy (EDX) detector and a BRUKER e-FlashHR electron backscatter diffraction (EBSD) detector was used to study both polished and deep etched samples. For EBSD characterization, an accelerating voltage of 20 kV, working distance of 15 mm, aperture size of 120 mm , and beam current 80 μA were used. Bruker ESPRIT 2.1 software was used to index the obtained EBSD patterns. EBSD datasets were analysed using MATLAB™ 9.2 (Mathworks, USA) based on the MTEX 5.1 toolbox. Throughout this paper, all unit cell wireframes in Figures were plotted from Euler angles measured by EBSD.

Geometric models of the crystal morphology and terminating facets observed in SEM imaging after deep etching were recreated in Matlab by one of two methods. In method one, the EBSD-measured orientation of a particle was used to define the orientation of the coordinate system and facets were then generated by plotting the chosen plane families for the point group symmetry, and tuning the distance from the centroid to each facet to best match the deep-etched SEM images. In method two, the EBSD step was skipped and the orientation was determined from the edge vectors between facets in SEM imaging, assuming that the facet families were the same as for particles studied in method 1.

3. Results and Discussion

3.1. Al-Mn IMCs after solidification and after solution heat treatment

Throughout this work, both after solidification of AZ31 and AZ80/AZ91 and after solution heat treatment of AZ80/AZ91, only two Al-Mn IMCs were detected: Al_8Mn_5 and $Al_{11}Mn_4$. These IMCs could be readily distinguished from each other and from other reported Al-Mn compounds by combining EBSD with EDS measurements. An example from a solution heat treated AZ80/AZ91 sample held at 410°C for 3 days is given in Fig. 2. EDS mapping in Fig. 2(a) shows a core-shell particle where the shell has higher Al content and lower Mn content than the core, which is quantified from EDS point analysis in Table 1. The two phases also have distinctly different greyscales in backscattered electron images (Fig. 2 (b)). EBSD mapping of the same core-shell particle is shown in Fig. 2(c). The phase map shows an $Al_{11}Mn_4$ shell around an Al_8Mn_5 core consistent with the EDS analysis in Fig. 2 (a) and Table 1.

Table 2 summarises the crystallographic details of Al_8Mn_5 and $Al_{11}Mn_4$ used for EBSD indexing and lattice matching analyses, along with references to the original crystallographic studies. Since $Al_{11}Mn_4$ is triclinic, there are various choices for the unit cell; here, we use the unit cell of Kontio et al.[46]. As shown in Table 2, Al_8Mn_5 is a rhombohedral gamma brass with strukturbericht designation $D8_{10}$ and can be described using three unit cells: the hexagonal setting with space group R3mH; the primitive rhombohedral setting R3mR; and a body centred rhombohedral (BCR) unit cell that is not a Bravais lattice but is useful since it has $\alpha \sim 89.1°$ and is a small distortion from the well-known body centred cubic gamma brass with the Cu_5Zn_8 prototype (strukturbericht designation $D8_2$) [47–50]. Further details on the three ways of describing the Al_8Mn_5 crystal and the interrelationships between the three unit cells are

given in ref [9]. In this paper, we index Al_8Mn_5 using the BCR unit cell to highlight the pseudo-cubic symmetry.

3.2. Al_8Mn_5 growth crystallography during solidification

During solidification, Al_8Mn_5 grew as equiaxed polyhedral particles and as rods. All equiaxed Al_8Mn_5 particles examined were cyclic twinned, similar to the study of Zeng et al. [9], whereas rod-like Al_8Mn_5 were single crystals along most of their length.

Even though Fig. 2 has been solution heat treated, the Al_8Mn_5 core is a typical example of a cyclic twinned equiaxed Al_8Mn_5 particle that formed during solidification. Fig. 2(d) is an IPF-Y map of the Al_8Mn_5 core. Note that different IPF colour keys are chosen throughout this paper to better distinguish crystal orientations. The cyclic twinning can be seen in the pole figures in Fig. 2(d): (i) the $\{111\}_{BCR}$ pole figure confirms the presence of four orientations labelled 1-4; (ii) the $\{100\}_{BCR}$ pole figure contains all four orientations (colours) overlapping at each spot, indicating ~90° rotations around the three <100> axes; and (iii) the $\{110\}_{BCR}$ and $\{1\bar{1}0\}_{BCR}$ pole figures each contain six spots with two orientations (colours) overlapping at each spot. A geometric model of the cyclic twin is shown in Fig. 2(f) by plotting the orientations as unit cell wire frames and assigning a different colour to each orientation following the IPF-Y colour key. Fig. 2(f) appears as eight cubes but the unit cells are rhombohedrons with angle α~ 89.1° and, when plotted like this, the unit cells share common $\{100\}_{BCR}$ planes. In Fig. 2(f), the upper image is the orientation of the cyclic twin plotted from the measured Euler angles with reference to a sectioning plane (i.e. the EBSD mapping surface), and the middle image is a normal view to the digital section into the cyclic twin. Comparing this digital section with the EBSD map in Fig. 2(d), it can be seen that the interfaces are consistent with $\{100\}_{BCR}$. This can

be further seen in Fig. 2(d) where white arrows have been added to indicate the internal interface normal vectors projected in this cross-section, and these have been superimposed on the $\{100\}_{BCR}$ pole figure in Fig. 2(e).

After solidification at the higher cooling rate, Al-Mn particles were Al_8Mn_5 with traces of $Al_{11}Mn_4$ on their surface. SE-images of equiaxed polyhedral Al_8Mn_5 particles are shown in Fig. 3 (a)-(c) after solidification at ~1 $K{\cdot}s^{-1}$ followed by deep etching. Since these cyclic-twinned particles have an overall pseudo-cubic symmetry, their equiaxed morphology and terminating facets can be understood from geometric models using plane families with cubic symmetry. It was measured in ref. [9] that cyclic-twinned Al_8Mn_5 particles commonly have {100}, {110}, and {112} facets, and the geometric models in Fig. 3 were generated within Matlab from the same cubic plane families, coloured orange, grey and blue respectively.

Fig. 3(g-h) shows Al_8Mn_5 pole figures from EBSD on a small region consisting of just one orientation in the cyclic-twinned particle in Fig. 3 (i). Comparing the pole figures from one orientation in Fig. 3(g), with pole figures from mapping a whole cyclic twinned particle containing four orientations in Fig. 2 highlights the fact that $\{110\}_{BCR}$ and $\{1\bar{1}0\}_{BCR}$ are two distinct families in Al_8Mn_5 and that these are combined into one pseudo-cubic family in cyclic twinned particles. For the geometric models, the pseudo-cubic symmetry can be obtained by merging the $\{110\}_{BCR}$ and $\{1\bar{1}0\}_{BCR}$ as has been done in Fig. 3(h), and also merging the $\{112\}_{BCR}$, $\{11\bar{2}\}_{BCR}$, $\{1\bar{1}2\}_{BCR}$.

3.3. $Al_{11}Mn_4$ nucleation and growth on Al_8Mn_5 during solidification

Inspecting the SEM images in Fig. 3, it can be seen that many of the Al_8Mn_5 particles contain traces of $Al_{11}Mn_4$ on their surfaces after solidification (Fig. 3 (b),(c), (e), (f)). In Fig. 3, $Al_{11}Mn_4$ is growing either as numerous islands (Fig. 3 (b) and (e)) or as long 'ropes' that are the

beginning of plate growth (Fig. 3 (c) and (f)). It was possible to find regions with no $Al_{11}Mn_4$, such as the images in Fig. 3 (a) and (d), but careful searching in the SEM usually revealed some trace of $Al_{11}Mn_4$ on Al_8Mn_5 particles.

Fig. 3(i) and (k) show that $Al_{11}Mn_4$ regions on Al_8Mn_5 tend to be elongated along one or two preferred directions on each {110} and $\{1\bar{1}0\}$ facet of Al_8Mn_5 (grey facets). In Fig. 3 (i) and (k), these directions are marked by vectors that are coloured the same when they are near parallel in the SE-image. It is reasonable to treat them as 3D vectors in SE-images since the $Al_{11}Mn_4$ islands and 'ropes' can be approximated as 1-D lines on a flat surface. The coloured 3D vectors are then superimposed in the BCR unit cell of Al_8Mn_5 measured by EBSD, which shows that all $Al_{11}Mn_4$ ropes/islands are consistent with being aligned with $<111>_{pseudo\text{-}cubic}$ of Al_8Mn_5.

From Fig. 3, it can be concluded that $Al_{11}Mn_4$ nucleate as numerous islands on both the $\{110\}_{BCR}$ and $\{1\bar{1}0\}_{BCR}$ facets (grey facets) of cyclic-twinned Al_8Mn_5 particles and, in the initial stages, grow along the $<111>_{pseudo\text{-}cubic}$ of Al_8Mn_5 on those facets. Comparing with the Scheil solidification path in Fig. 1, the presence of $Al_{11}Mn_4$ on the surface of Al_8Mn_5 after solidification is consistent with the partial quasi-peritectic reaction, L + Al_8Mn_5 → α-Mg + $Al_{11}Mn_4$.

More $Al_{11}Mn_4$ formed on Al_8Mn_5 during solidification at the slower cooling rate in this work, even in samples that were switched to the faster cooling method from 430 °C to minimise solid-state transformations after solidification. At the same time, it was found that for the same cooling conditions and within the same sample, the amount of $Al_{11}Mn_4$ growing on Al_8Mn_5 particles was highly variable, with some Al_8Mn_5 particles having only traces of $Al_{11}Mn_4$ (e.g. Fig. 3) and others being fully covered by $Al_{11}Mn_4$. By examining Al_8Mn_5 particles with increasing amounts of surrounding $Al_{11}Mn_4$, information could be obtained on how $Al_{11}Mn_4$

grew around Al_8Mn_5. Fig. 4 is an example where the $Al_{11}Mn_4$ developed into numerous faceted plates surrounding an Al_8Mn_5 particle. In order to determine the crystallographic facets of the plates, EBSD mapping was performed directly on top of the $Al_{11}Mn_4$ plates at appropriate tilt angles (ranging from 45-75°) where satisfactory Kikuchi patterns could be collected. Fig. 4 (a,e) shows the raw EBSD measurements on exposed $Al_{11}Mn_4$ crystals after removing α-Mg using selective etching. The IPF-Y colour scheme is used in Fig. 4 (a,e). Since the Euler angles from EBSD are calculated from the 0° tilt stage, images of the same area taken at the normal view (stage at 0°) are shown in Fig. 4 (b,f). The rectangles in Fig. 4 (b,f) are coloured based on the EBSD measurements and positioned carefully with reference to the raw maps. In Fig. 4 (b,f), arrows have been superimposed normal to each $Al_{11}Mn_4$ plate for which EBSD data was gathered. This could be done with reasonable accuracy because these plates are nearly vertical as can be seen in the whole crystals in Fig. 4 (c,g). In Fig. 4 (d,h), the arrows are superimposed on the $\{010\}_{Al11Mn4}$ pole figures. Since $Al_{11}Mn_4$ is triclinic, $P\bar{1}$, there is one member of the {010} family in the northern hemisphere, and each spot in the pole figure represents one orientation. The {010} plane is plotted for eleven plates but only six arrows are superimposed since some plates have the same/similar plate normal directions. For all six arrows, the eleven plate normals are consistent with the $\{010\}_{Al11Mn4}$ plane normal, showing that the $Al_{11}Mn_4$ plates are bounded by $\{010\}_{Al11Mn4}$ facets. This is consistent with {010} or {040} being the closest packed plane in triclinic $Al_{11}Mn_4$ [46].

3.4. Orientation relationships and twins

$Al_{11}Mn_4$ plates usually had reproducible orientation relationships (ORs) with the underlying Al_8Mn_5. As an example, Fig. 5(a) contains the cross-section of a single crystal Al_8Mn_5 rod partially covered by $Al_{11}Mn_4$ plates. A 3D example of a similar hexagonal Al_8Mn_5 rod can be

found in SI-Fig. 4, where the long Al_8Mn_5 side facets were measured as $\{1\bar{1}0\}_{BCR}$. Fig. 5 (b) shows the EBSD IPF-Z map of both the single crystal Al_8Mn_5 rod and multiple $Al_{11}Mn_4$ parallel plate orientations. Fig. 5 (c) confirms that the main growth facets of $\{010\}Al_{11}Mn_4$ are not parallel to any $\{110\}_{BCR}$ or $\{1\bar{1}0\}_{BCR}$ planes of the Al_8Mn_5 rod, which is important for the ORs discussed later. Fig. 5 (d) shows pole figures of parallel planes and directions between Al_8Mn_5 and four different $Al_{11}Mn_4$ orientations, where circles are marked in fixed positions to demonstrate the parallelisms between pairs.

The pole figure in Fig. 5 (c) shows that the $Al_{11}Mn_4$ plates all share a near parallel {010} and, in Fig. 5 (d), it can be seen that the $\{110\}_{BCR}$ and $\langle 1\bar{1}1\rangle_{BCR}$ of Al_8Mn_5 are near parallel with different pairs of $Al_{11}Mn_4$ planes and directions in the four distinct $Al_{11}Mn_4$ orientations. Of these, the $\{01\bar{1}\}_{Al11Mn4}$ and $\langle 0\bar{1}\bar{1}\rangle_{Al11Mn4}$ were often more parallel with their Al_8Mn_5 counterparts, and this is defined here as OR-A1. The other $Al_{11}Mn_4$ orientations in Fig. 5 are defined as ORs-A2…4 as annotated on Fig. 5(d).

To ensure that EBSD patterns were correctly indexed and that ORs were correctly identified, the EBSD patterns were further analysed by carrying out cross-correlation between experimental patterns and dynamical simulated patterns within Bruker DynamicS. Fig. 5(e) shows selected experimental EBSD patterns and the best-fitting simulated patterns. The CCC values are cross-correlation coefficients of the best-fitting pattern. For example, for the Al_8Mn_5 pattern (top), the CCC is 0.61 as compared to CCC values of 0.47, 0.54 and 0.50 for the next-best patterns (not shown) that are similar due to the cubic pseudo-symmetry but are distinguishable. Similarly, the CCC values of correct $Al_{11}Mn_4$ orientations were in the range of 0.46-0.58 compared with a CCC < 0.2 for the next-best $Al_{11}Mn_4$ orientation solutions. More examples of Kikuchi patterns and distinguishing between orientations and phases by

dynamical simulations can be found in SI-Fig. 1-2. Given acceptable Kikuchi patterns (e.g. the ones in Fig. 5(e)), it was found that the low crystal symmetry (triclinic) of $Al_{11}Mn_4$ ensures that EBSD is well suited to measure the $Al_{11}Mn_4$ orientations correctly.

Selected parallel bands and zone axes in the Kikuchi patterns are also marked on in the final column of Fig. 5(e). Those relevant to Al_8Mn_5-$Al_{11}Mn_4$ ORs are highlighted in yellow, whereas the near-parallel $\{010\}_{Al11Mn4}$ band/planes are highlighted in pink for the four $Al_{11}Mn_4$ orientations.

Fig. 6(a) summarises orientation relationship OR-A1 between $Al_{11}Mn_4$ and Al_8Mn_5, showing stereographic projections of Al_8Mn_5 in both the BCR and R-3mH settings and that of $Al_{11}Mn_4$ with the OR-A1 orientation. Note that since the EBSD approach used here does not handle the polar point groups properly, the families of Al_8Mn_5 planes and directions are coloured in a R-3mH setting instead of its actual polar R3mH space group for simplicity and practicality. Note that selected relatively-close packed $Al_{11}Mn_4$ planes are shown in Fig. 6(a-b) to highlight that these are near-parallel to the closest packed planes in Al_8Mn_5. All 11 closest-packed $Al_{11}Mn_4$ planes with similar structure factors are listed in SI-Table 1, including a low-index $\{010\}Al_{11}Mn_4$ plane which is parallel in the four $Al_{11}Mn_4$ orientations. Orientation relationship OR-A1 can be written as $(\ \bar{1}\bar{1}0\ )_{Al8Mn5\_BCR}||(\ 0\bar{1}1\ )_{Al11Mn4}$ (or identically $(\ 110\ )_{Al8Mn5\_BCR}||(\ 01\bar{1}\ )_{Al11Mn4}$) with the common directions being $[\ 1\bar{1}1\ ]_{Al8Mn5\_BCR}$ || $[0\bar{1}\bar{1}]_{Al11Mn4}$. Because of the non-rotational symmetry of P-1 $Al_{11}Mn_4$, all the variants for this OR-A1 are simply due to the rotational symmetry operations for Al_8Mn_5, which has 6 rotational symmetry elements for the R-3mH setting. Therefore, there are 6 variants for OR-A1 between parent Al_8Mn_5 and child $Al_{11}Mn_4$, $\{110\}_{Al8Mn5\_BCR}||\{\ 01\bar{1}\ \}_{Al11Mn4}$ with $\langle 1\bar{1}1\rangle_{Al8Mn5\_BCR}$ || $\langle 0\bar{1}\bar{1}\rangle_{Al11Mn4}$, listed in Table 3. The planar lattice match of OR-A1 is shown

in Fig. 6(c), where the origins at the centre are chosen to be the Al5 site of Al_8Mn_5 (R3mH setting) and Al1 site of $Al_{11}Mn_4$, with a mismatch value of ~1% using the Bramfitt method [51] after projecting atoms into the plane.

In Table 3 and related Al_8Mn_5 stereographic projections, the conversion between BCR and R3mH settings of Al_8Mn_5 planes and directions were calculated using the following two matrix operations based on [52].

$$[h,k,l]_{HEX} = [h,k,l]_{BCR} * \begin{bmatrix} -1 & 0 & 1/2 \\ 1 & -1 & 1/2 \\ 0 & 1 & 1/2 \end{bmatrix} \quad \text{Eq. 1}$$

$$[u,v,w]_{HEX} = [u,v,w]_{BCR} * \begin{bmatrix} -2/3 & -1/3 & 2/3 \\ 1/3 & -1/3 & 2/3 \\ 1/3 & 2/3 & 2/3 \end{bmatrix} \quad \text{Eq. 2}$$

The OR-As were the most frequent OR measured around Al_8Mn_5 particles with a probability greater than 60% (14/22 Al_8Mn_5 particles found with OR-As). Another set of ORs (OR-Bs) was also identified, which were less commonly measured (4/22 Al_8Mn_5 particles, <~20%). An example of EBSD measurement for OR-Bs can be found in SI-Fig. 6. Fig. 7(a) shows the stereographic projections for OR-B1, where $(0\bar{1}0)Al_{11}Mn_4$ is parallel with $(\bar{1}01)Al_8Mn_5$ while $[\bar{1}0\bar{2}]_{Al11Mn4\_BCR}$ is parallel with $[1\bar{1}1]_{Al8Mn5BCR}$. Here it is convenient to define OR-Bs using the growth facets of $\{010\}_{Al11Mn4}$ and $\{\bar{1}01\}_{Al8Mn5\ BCR}$, although they are not necessarily the interfaces between $Al_{11}Mn_4$ and Al_8Mn_5. Fig. 7(b) shows four $Al_{11}Mn_4$ orientations, in a similar manner to those in Fig. 6(b) and (d). OR-B1 can be written as $\{-101\}_{Al8Mn5\_BCR}||\{0\text{-}10\}_{Al11Mn4}$ with $<1\text{-}11>_{Al8Mn5\_BCR}$ || $<\text{-}10\text{-}2>_{Al11Mn4,}$ with six variants as summarized in Table 3. For the lattice match in Fig. 7(c), OR-B1 also has a good local Bramfitt disregistry value of ~2% on the edges of the black rectangle (a size equivalent to a $(-101)_{Al8Mn4\text{-}BCR}$ plane). However, the overall atom-on-atom matching is slightly worse compared to that of OR-A1, which may make OR-B1

less favored than OR-A1. We note that there may be additional preferred ORs between Al_8Mn_5 and $Al_{11}Mn_4$ involving {100} or {112} BCR Al_8Mn_5 facets in our EBSD datasets but these were not considered sufficiently reproducible for us to study in detail here.

As well as being related to Al_8Mn_5 by simple ORs (e.g. A1 and B1), the surrounding $Al_{11}Mn_4$ plates were often related to each other by twinning operations, as is the case for the four $Al_{11}Mn_4$ orientations in Fig. 5(b), Fig. 6(a,b) and Fig. 7(a,b). The mutual twinning relationships in $Al_{11}Mn_4$ are shown graphically in Fig. 6(d) and are consistent with the four $Al_{11}Mn_4$ stereographic projections in Fig. 6(a,b). Fig. 6(d) shows that, for the #1 and #2 $Al_{11}Mn_4$ orientations (OR-A1 and A2), the red a-axis $[100]_{Al11Mn4}$ in #1 is parallel with $[-100]_{Al11Mn4}$ in #2 while the $\{010\}Al_{11}Mn_4$ normals are facing the same direction. This is defined as twinning type I, where #1 and #2 (also #3 and #4) are related by a 180° rotation along the $\{010\}_{Al11Mn4}$ twin plane normal, forming {010} reflection twins. There is additionally a twinning type II between #2 and #3 involving a 180° rotation around a $\langle 10\bar{1} \rangle$ axis, leaving $[-100]_{Al11Mn4}$ parallel with $[001]_{Al11Mn4}$ and the $\{010\}_{Al11Mn4}$ plane normals facing each other. The two types of $Al_{11}Mn_4$ twinning both share contact planes of $\{010\}_{Al11Mn4}$, which are the $Al_{11}Mn_4$ facets and the interfaces between neighbouring $Al_{11}Mn_4$ plates in Fig. 4 and Fig. 5. Such $Al_{11}Mn_4$ twinning relationships are also found in OR-Bs as can be seen by comparing Fig. 7(a) and (b). Note that two $Al_{11}Mn_4$ variants (v1 and v2) of OR-B1 are also mutual twins with the $Al_{11}Mn_4$ type-I twinning (see stereograms for OR-B1 and OR-B2*). The OR-B2* is thus not a new OR-B because it is just a variant of OR-B1(v2), so as OR-B3* being a variant of OR-B4* or vice versa.

While most $Al_{11}Mn_4$ grew on the surface of Al_8Mn_5 particles during solidification, some $Al_{11}Mn_4$ grew as long plates that were often twinned with the same type II twinning as in Fig. 6(d). An example is shown in Fig. 8. The IPF-Z map in Fig. 8 (b) shows this plate contains two

orientations (colours), and the two triclinic $Al_{11}Mn_4$ wireframe unit cells have been plotted from the measured orientations in Fig. 8(a). Note that the 180° rotation around $<10\bar{1}>_{Al11Mn4}$ makes the two $Al_{11}Mn_4$ twins coincide in the $\{010\}_{Al11Mn4}$ plane but with swapped a and c axes, which is due to the small difference (<1%) between the lattice parameters a and c of $Al_{11}Mn_4$ (Table 2).

The ORs between $Al_{11}Mn_4$ and Al_8Mn_5 and the multiple twinned $Al_{11}Mn_4$ orientations surrounding Al_8Mn_5 particles could have formed by two mechanisms: (A) $Al_{11}Mn_4$ orientations could have formed by nucleation on Al_8Mn_5 with multiple ORs or variants, followed by $Al_{11}Mn_4$ plate growth until plates impinged on their neighbours to give a twin OR; and (B) the twinned $Al_{11}Mn_4$ orientations may have formed by growth twinning. Mechanism A seems to occur because multiple discrete islands of $Al_{11}Mn_4$ could be observed on the different Al_8Mn_5 facets in the early stages of $Al_{11}Mn_4$ formation (Fig. 3). Mechanism B is also likely, especially since the main growth facet of each $Al_{11}Mn_4$ plate, {010}, (Fig. 4) is the interface plane (Fig. 5) in the two twin types for $Al_{11}Mn_4$. It may be that the Al_8Mn_5-$Al_{11}Mn_4$ OR with the best lattice match (e.g. OR-A1 in Fig. 5 and 6(a-c)) was the nucleation OR, and the worse matching Al_8Mn_5-$Al_{11}Mn_4$ ORs (e.g. ORs A3 and A4 in Fig. 5 and 6(a-c)) formed when subsequent $Al_{11}Mn_4$ growth twins grew over the Al_8Mn_5 crystal. However, further work is required to confirm this.

3.5. Solid state transformation from Al_8Mn_5 to $Al_{11}Mn_4$ at 410°C

Fig. 9 shows representative 2D cross-sections of the core-shell particles at a series of ageing times at 410°C. These are backscattered electron micrographs where the α-Mg appears black and Al_8Mn_5 is brighter than $Al_{11}Mn_4$ due to the higher Mn content. As time

progressed, a shell of $Al_{11}Mn_4$ developed around the Al_8Mn_5 core and the shell then grew to consume the core, transforming all Al_8Mn_5 into $Al_{11}Mn_4$.The morphology formed during heat treatment is not the same as the that formed during solidification. $Al_{11}Mn_4$ that grew into liquid often had a simple plate morphology (e.g. Fig. 4 and Fig. 5), whereas $Al_{11}Mn_4$ formed during heat treatment had a more globular shape and numerous cracks mostly filled with α-Mg (Fig. 9).

The volume expansion leading to this cracking can be understood with the following calculations. At 410 °C, we start with a three-phase mixture of (Mg)+ $Mg_{17}Al_{12}$+ Al_8Mn_5 and two distinct phase transformations occur: (1) the $Mg_{17}Al_{12}$ dissolves into the (Mg), and (2) the Al_8Mn_5 transforms into $Al_{11}Mn_4$. Since the Mn content in both (Mg) and $Mg_{17}Al_{12}$ is essentially zero [31,32], transformation (1) can be reasonably neglected noting that the initial (Mg)+$Mg_{17}Al_{12}$ mixture composition will be equal to the single phase (Mg) composition after $Mg_{17}Al_{12}$ dissolution. For transformation (2), the phase fractions and phase compositions can be found by a molar balance between the (Mg) matrix and the relevant IMC using the lever rule in Eq. 3. Note that, before $Mg_{17}Al_{12}$ dissolves, Eq. 3 can be modified so that $f_{(Mg)}$ is replaced with $f_{(Mg)} + f_{Mg17Al12}$, and $X_{(Mg)}$ is replaced with the mixture composition $\bar{X}_{(Mg)+Mg17Al12}$:

$$f_{(Mg)} = \frac{X_0 - X_{IMC}}{X_{(Mg)} - X_{IMC}} \qquad \text{Eq. 3}$$

Where f is the mole fraction of phase, and X indicates composition in mole fraction. Eq. 3 is one equation with two unknowns, $f_{(Mg)}$ and $X_{(Mg)}$. However, in Mg-9Al-xMn alloys, the composition of Mn in the (Mg) phase at 410°C is on the order 10^{-6} mol fraction [31,32] and can be approximated as zero, allowing $f_{(Mg)}$ to be solved in Eq. 3. This value of $f_{(Mg)}$ can then be used to calculate the compositions of Al and Mg in $X_{(Mg)}$. The results of this approach are

given in Table 5 where Al_8Mn_5 and $Al_{11}Mn_4$ have been approximated as stoichiometric compounds. The resulting values in Table 5 are only subtly different to calculations in Thermo-Calc and Pandat that do not make these simplifying assumptions [31,32]. Table 5 also shows conversions into mass fractions and volume fractions of phases. Theoretical densities from the crystal structures [46,48] were used for the IMCs. The densities of α-Mg were taken from JMatPro [53] for the two α-Mg compositions in Table 5.

It can be seen in Table 4 that both the Al content in α-Mg and the phase fraction of α-Mg decrease as Al solute in α-Mg reacts with 4 moles of Al_8Mn_5 to produce 5 moles of $Al_{11}Mn_4$. This transformation leads to an increase in IMC volume of $(V_{Al11Mn4} - V_{Al8Mn5})/ V_{Al8Mn5} \approx 47\%$, which is mostly caused by the increased Al content in the IMC since the interatomic distances in $Al_{11}Mn_4$ are similar to those in Al_8Mn_5 as shown in Fig. 6(c).

Fig. 9 (a) and (b) are schematics of the core-shell transformation of an Al_8Mn_5 particle into $Al_{11}Mn_4$ where L>R due to volume expansion in the shell. To study the kinetics of this solid-state transformation at 410 °C, the 2D area fractions of $Al_{11}Mn_4$ phase were measured from at least 100 particles (e.g. Fig. 9) at each heat treatment time. Fig. 10(c) shows the equivalent circular diameter (ECD) measurements of the total size of Al_8Mn_5 core and $Al_{11}Mn_4$ shell after 6 days heat treatment. Fig. 10 (d) sees an increasing trend for the total ECDs (open symbols) after different aging times and relatively constant converted sizes of prior Al_8Mn_5 particle sizes (solid symbols). The mean of the measured 2D area fractions of $Al_{11}Mn_4$, $\overline{A_A}$, at each time was converted to the volume fraction of original Al_8Mn_5 transformed, α, accounting for the volumetric expansion and assuming the geometry of spherical core-shell particles using Eq. 4. This conversion is shown graphically in Fig. 10 (e)

and is derived in SI-section 5. z is the ratio of the volume of $Al_{11}Mn_4$ to that of Al_8Mn_5 (~1.47).

$$\overline{A_A} = 1 - \left\{ \left(\frac{1-\alpha}{1-\alpha+z\alpha}\right)^{\frac{1}{3}} - \frac{1-\left(\frac{1-\alpha}{1-\alpha+z\alpha}\right)^{\frac{2}{3}}}{2} \ln\left(\frac{1+\left(\frac{1-\alpha}{1-\alpha+z\alpha}\right)^{\frac{1}{3}}}{1-\left(\frac{1-\alpha}{1-\alpha+z\alpha}\right)^{\frac{1}{3}}} \right) \right\} \quad \text{Eq. 4}$$

The fraction transformed data are plotted versus time in Fig. 10 (f) and have been fit using the Johnson-Mehl-Avrami-Kolmogorov (JMAK) equation with a JMAK exponent of n~1.5. A key feature is that the kinetics are relatively slow, taking approximately one week to transform most Al_8Mn_5 into $Al_{11}Mn_4$ at 410 °C for the initial particle size of ~8 ± 2 μm (Fig. 10(d)).

Solid state transformations of core-shell particles involve (i) the nucleation of the shell phase; (ii) the propagation of interfaces as the shell phase grows at the expense of the core phase; and (iii) diffusion through the growing shell to bring species (e.g. Al and Mn) to the interfaces where they react. Typically, one of these phenomena is rate controlling and analytical models have been developed for each phenomenon. Three models are given in Eq. 5-7 that each assumes spherical core-shell particles transforming from the surface inwards, where α is the volume fraction transformed, t is the time, k is a constant, and z is the ratio of the volume of product to the volume of reactant (1.47 for 4 moles of Al_8Mn_5 transforming into 5 moles of $Al_{11}Mn_4$). Eq. 5 is for phase boundary reaction control [54–56], Eq. 6 is for shell-diffusion control [57] and Eq. 7 is for shell-diffusion control accounting for volume changes [58,59].

$$1 - (1-\alpha)^{\frac{1}{3}} = kt \quad \text{Eq. 5}$$

$$1 - \frac{2}{3}\alpha - (1-\alpha)^{\frac{2}{3}} = kt \quad \text{Eq. 6}$$

$$z/(z-1) - (1-\alpha)^{\frac{2}{3}} - [1+(z-1)\alpha]^{\frac{2}{3}}/(z-1) = kt \qquad \text{Eq. 7}$$

The fraction transformed data from Fig. 10 (f) are compared with these models in Fig. 10 (g) by plotting the fraction transformed against reduced time, $t/t_{0.5}$, where $t_{0.5}$ is the time when half the original Al_8Mn_5 volume has transformed. Our data are consistent with phase boundary reaction control. It was also found that, if the volume expansion is ignored and even if both the volume expansion and the 2D → 3D conversion in Fig. 10 (e) are ignored, the fraction transformed versus reduced time plot in Fig. 10 (g) is only slightly changed and remains consistent with phase boundary-controlled growth. Based on the degree of cracking in the $Al_{11}Mn_4$ shell (Fig. 9), strain associated with the volume expansion is likely contributing to limiting the motion of $Al_{11}Mn_4/Al_8Mn_5$ interfaces, in addition to the change of complex crystal structure as the interface advances with a relatively good lattice match at interfaces (Fig. 6). Since Al from the α-Mg matrix takes part in the transformation of Al_8Mn_5 into $Al_{11}Mn_4$, it is expected that the local Al content in the α-Mg will also affect the transformation.

In most particles, the transformation occurred with a 'shrinking core' geometry similar to Fig. 9. However, occasionally, the core-shell reaction occurred with $Al_{11}Mn_4$ growing preferentially along Al_8Mn_5 twin boundaries, dividing the cyclic twinned Al_8Mn_5 into discrete single crystal regions separated by $Al_{11}Mn_4$. An example of this is given in Fig. 11. Note that the EBSD IPF map of the four Al_8Mn_5 twins in Fig. 11(b), the calculated cross-section in Fig. 11(c), and the Al_8Mn_5 pole figures in Fig. 11(d) show the same cyclic twin characteristics as those in Fig. 2.

A typical industrial solution heat treatment time for AZ80/AZ91 is 20 hours at which point most $Mg_{17}Al_{12}$ has dissolved [17] but only ~10 vol% of Al_8Mn_5 had transformed in Fig. 10. At

this stage of the core-shell reaction, $Al_{11}Mn_4$ formed a contiguous shell that encapsulates Al_8Mn_5 and removes all interfaces between Al_8Mn_5 and (Mg) (Fig. 9). Since Al-Mn IMCs with higher Al:Mn ratios are reported to act as less efficient micro-cathodes in the α-Mg matrix and, thus, decrease the corrosion rate [44,45], an $Al_{11}Mn_4$ shell may be beneficial to corrosion performance. At the same time, as shown in Fig. 9, longer times caused more cracking of the $Al_{11}Mn_4$ shell which greatly increased the interfacial area between (Mg) and $Al_{11}Mn_4$. In future, it will be interesting to study the relative importance of the changing Al-Mn particles versus the changing $Mg_{17}Al_{12}$ phase on corrosion performance after solutionising.

4. Conclusions

The crystallography and kinetics of $Al_{11}Mn_4$ formation on Al_8Mn_5 has been studied during the solidification of Mg-3Al-1Zn-0.5Mn and Mg-9Al-0.7Zn-0.2Mn and the solution heat treatment of Mg-9Al-0.7Zn-0.2Mn (wt%).

During solidification, Al_8Mn_5 grew as either cyclic twinned equiaxed particles similar to Zeng et al. [9] or as hexagonal rods. $Al_{11}Mn_4$ only formed as small traces unless very low cooling rates were applied (here ~0.1 K/s). $Al_{11}Mn_4$ nucleated mostly on the $\{110\}_{BCR}$ and $\{1\bar{1}0\}_{BCR}$ facets of Al_8Mn_5 and initially grew along $\langle 1\bar{1}1\rangle_{BCR}$ of Al_8Mn_5. During solidification, $Al_{11}Mn_4$ developed into plates with (010) facets.

$Al_{11}Mn_4$ had multiple related orientation relationships (ORs) with Al_8Mn_5, that could be split into two sets of ORs related with OR-A1 and OR-B1:

$$(110)^{BCR}_{Al8Mn5} \parallel (01\bar{1})_{Al11Mn4} \text{ and } [1\bar{1}1]^{BCR}_{Al8Mn5} \parallel [0\bar{1}\bar{1}]_{Al11Mn4} \qquad \text{OR-A1}$$

$$(\bar{1}01)^{BCR}_{Al8Mn5} \parallel (0\bar{1}0)_{Al11Mn4} \text{ and } [1\bar{1}1]^{BCR}_{Al8Mn5} \parallel [\bar{1}0\bar{2}]_{Al11Mn4} \qquad \text{OR-B1}$$

Neighbouring $Al_{11}Mn_4$ plates were often twinned. The twin relationships could form by growth twinning and/or multiple $Al_{11}Mn_4$ nucleation events on Al_8Mn_5 with different related orientation relationships and variants. The two $Al_{11}Mn_4$ twinning relationships are:

Type I: 180° rotation around the {010} plane normal, forming {010} reflection twins

Type II: 180° rotation around $<10\bar{1}>$ with {010} contact plane. This involves the swapping of the a and c axes, which differ in length by <1%.

These features of $Al_{11}Mn_4$ formation on Al_8Mn_5 were similar in AZ80/AZ91 and AZ31.

During solution heat treatment at 410 °C, Al_8Mn_5 equiaxed particles transformed into $Al_{11}Mn_4$ by a core-shell reaction with cracking in the $Al_{11}Mn_4$ shell due to the volume expansion when 4 moles of Al_8Mn_5 react with Al solute from the (Mg) phase to produce 5 moles of $Al_{11}Mn_4$. Analysis of the reaction kinetics showed the data are consistent with a phase boundary-controlled reaction.

The results provide insights into $Al_{11}Mn_4$ in AZ31 and AZ91/AZ80 used in industry. (i) In the as-cast condition, the lack of $Al_{11}Mn_4$ is due to the relatively high cooling rates applied during casting processes such as HPDC and direct chill casting. (ii) In solution heat treated alloys, Al-Mn particles generally contain only a shell of $Al_{11}Mn_4$ around Al_8Mn_5 particles because the solid-state reaction kinetics at 410 °C are relatively slow compared with the time of a typical solution heat treatment (~20 hours). However, this time is sufficient for a contiguous $Al_{11}Mn_4$ shell to form, shielding the (Mg) matrix from the Al_8Mn_5 phase which may be important for corrosion performance.

Acknowledgements

Financial support from EPSRC (UK) under grant number EP/N007638/1 (the Future LiME Hub) is gratefully acknowledged. This work was partly supported by the National Natural Science Foundation of China (51904352). The authors acknowledge use of characterization facilities within the Harvey Flower Electron Microscopy Suite, Department of Materials, Imperial College London.

References

[1] ASTM B91, Standard Specification for Magnesium-Alloy forgings, Annu. B. ASTM Stand. (2017) 1–5.

[2] ASTM B80, Standard Specification for Magnesium-Alloy Sand Castings, Annu. B. ASTM Stand. (2015) 1–12.

[3] ASTM B94, Standard Specification for Magnesium-Alloy Die Castings., Annu. B. ASTM Stand. (2018) 1–6.

[4] B. Zhang, H. Liao, C. Coddet, Effects of processing parameters on properties of selective laser melting Mg–9%Al powder mixture, Mater. Des. 34 (2012) 753–758.

[5] A.K. Dahle, Y.C. Lee, M.D. Nave, P.L. Schaffer, D.H. StJohn, Development of the as-cast microstructure in magnesium–aluminium alloys, J. Light Met. 1 (2001) 61–72.

[6] M.Y. Wang, J.J. Williams, L. Jiang, F. De Carlo, T. Jing, N. Chawla, Three Dimensional (3D) Microstructural Characterization and Quantitative Analysis of Solidified Microstructures in Magnesium-Based Alloys, Metallogr. Microstruct. Anal. (2012).

[7] A. V. Nagasekhar, C.H. Cáceres, C. Kong, 3D characterization of intermetallics in a high pressure die cast Mg alloy using focused ion beam tomography, Mater. Charact. 61 (2010) 1035–1042.

[8] G. Zeng, S.S. Shuai, X.Z. Zhu, S.X. Ji, J.W. Xian, C.M. Gourlay, Al8Mn5 in High-Pressure Die Cast AZ91: Twinning, Morphology and Size Distributions, Metall. Mater. Trans. A. 51 (2020) 2523–2535.

[9] G. Zeng, J.W. Xian, C.M. Gourlay, Nucleation and growth crystallography of Al8Mn5 on B2-Al(Mn,Fe) in AZ91 magnesium alloys, Acta Mater. 153 (2018) 364–376.

[10] R.M. Wang, A. Eliezer, E. Gutman, Microstructures and dislocations in the stressed AZ91D magnesium alloys, Mater. Sci. Eng. A. 344 (2003) 279–287.

[11] V.Y. Gertsman, J. Li, S. Xu, J.P. Thomson, M. Sahoo, Microstructure and second-phase particles in low- and high-pressure die-cast magnesium alloy AM50, Metall. Mater. Trans. A Phys. Metall. Mater. Sci. 36 (2005) 1989–1997.

[12] C. Scharf, A. Ditze, A. Shkurankov, E. Morales, C. Blawert, W. Dietzel, K.U. Kainer, Corrosion of AZ 91 Secondary Magnesium Alloy, Adv. Eng. Mater. 7 (2005) 1134–1142.

[13] H. Krawiec, S. Stanek, V. Vignal, J. Lelito, J.S. Suchy, The use of microcapillary techniques to study the corrosion resistance of AZ91 magnesium alloy at the microscale, Corros. Sci. 53 (2011) 3108–3113.

[14] B. Mingo, R. Arrabal, M. Mohedano, C.L. Mendis, R. del Olmo, E. Matykina, N. Hort, M.C. Merino, A. Pardo, Corrosion of Mg-9Al alloy with minor alloying elements (Mn, Nd, Ca, Y and Sn), Mater. Des. 130 (2017) 48–58.

[15] T. Chen, Y. Yuan, T. Liu, D. Li, A. Tang, X. Chen, R. Schmid-Fetzer, F. Pan, Effect of Mn Addition on Melt Purification and Fe Tolerance in Mg Alloys, JOM. (2021).

[16] L.H. Han, H. Hu, D.O. Northwood, X. Nie, A Kinetic Model for Dissolution of Second Phases in Die-Cast Mg Alloy AM50, Defect Diffus. Forum. 297–301 (2010) 111–116.

[17] K. Kadali, D. Dubey, R. Sarvesha, H. Kancharla, J. Jain, K. Mondal, S.S. Singh, Dissolution Kinetics of Mg17Al12 Eutectic Phase and Its Effect on Corrosion Behavior of As-Cast AZ80 Magnesium Alloy, JOM. 71 (2019) 2209–2218.

[18] P. Palai, N. Prabhu, P.D. Hodgson, B.P. Kashyap, Grain Growth and β-Mg17Al12 Intermetallic Phase Dissolution During Heat Treatment and Its Impact on Deformation Behavior of AZ80 Mg-Alloy, J. Mater. Eng. Perform. 23 (2014) 77–82.

[19] T. Zhu, Z.W. Chen, W. Gao, Dissolution of Eutectic β-Mg17Al12 Phase in Magnesium AZ91 Cast Alloy at Temperatures Close to Eutectic Temperature, J. Mater. Eng. Perform. 19 (2010) 860–867.

[20] Y. Jiang, G. Tang, C. Shek, Y. Zhu, Z. Xu, On the thermodynamics and kinetics of electropulsing induced dissolution of β-Mg17Al12 phase in an aged Mg–9Al–1Zn alloy, Acta Mater. 57 (2009) 4797–4808.

[21] N.N. Aung, W. Zhou, Effect of heat treatment on corrosion and electrochemical behaviour of AZ91D magnesium alloy, J. Appl. Electrochem. 32 (2002) 1397–1401.

[22] O. Lunder, J.E. Lein, T.K. Aune, K. Nisancioglu, Role of Mg17Al12 phase in the corrosion of Mg alloy AZ91, Corrosion. 45 (1989) 741–748.

[23] G. Song, A.L. Bowles, D.H. StJohn, Corrosion resistance of aged die cast magnesium alloy AZ91D, Mater. Sci. Eng. A. 366 (2004) 74–86.

[24] J.F. Nie, Precipitation and hardening in magnesium alloys, in: Metall. Mater. Trans. A Phys. Metall. Mater. Sci., Springer, 2012: pp. 3891–3939.

[25] C.R. Hutchinson, J.F. Nie, S. Gorsse, Modeling the precipitation processes and strengthening mechanisms in a Mg-Al-(Zn) AZ91 alloy, Metall. Mater. Trans. A Phys. Metall. Mater. Sci. 36 (2005) 2093–2105.

[26] M.X. Zhang, P.M. Kelly, Crystallography of Mg17Al12 precipitates in AZ91D alloy, Scr. Mater. 48 (2003) 647–652.

[27] Z. Han, G. Han, A.A. Luo, B. Liu, Large-scale three-dimensional phase-field simulation of multi-variant β-Mg17Al12 in Mg-Al-based alloys, Comput. Mater. Sci. 101 (2015) 248–254.

[28] R. Sarvesha, U. ur R. Ghori, G. Thirunavukkarasu, Y.L. Chiu, I.P. Jones, J. Jain, S.S. Singh, A study on the phase transformation of γ2-Al_8Mn_5 to LT-$Al_{11}Mn_4$ during solutionizing in AZ91 alloy, J. Alloys Compd. 873 (2021) 159836.

[29] L. Lai, K. Zhang, M.L. Ma, G.L. Shi, Effect of heat treatment on microstructures and properties of AZ40M alloy, in: Mater. Sci. Forum, Trans Tech Publications Ltd, 2016: pp. 173–180.

[30] D. Dubey, K. Kadali, H. Kancharla, A. Zindal, J. Jain, K. Mondal, S.S. Singh, Effect of Precipitate Characteristics on the Corrosion Behavior of a AZ80 Magnesium Alloy, Met. Mater. Int. (2020).

[31] Thermo-Calc 2019a TCMG Database 4, (2019).

[32] Pandat 2018 with PanMg2018, (2019).

[33] J.H. Bae, B.S. You, Feasibility of grain refinement method for AZ91 alloy using commercial Al-SiC composite, Mater. Sci. Technol. 36 (2020) 194–201.

[34] T. Laser, M.R. Nürnberg, A. Janz, C. Hartig, D. Letzig, R. Schmid-Fetzer, R. Bormann, The influence of manganese on the microstructure and mechanical properties of AZ31 gravity die cast alloys, Acta Mater. 54 (2006) 3033–3041.

[35] C.J. Simensen, B.C. Oberlander, J. Svalestuen, A. Thorvaldsen, Determination of the Equilibrium Phases in Molten Mg-4 wt.% Al-Mn Alloys, Z. Met. 79 (1988) 537–540.

[36] C.J. Simensen, B.C. Oberlaender, J. Svalestuen, A. Thorvaldsen, Phase diagram for magnesium-aluminium-manganese above 650C, Z. Met. 79:11 (1988).

[37] Y. Du, J. Wang, J. Zhao, J.C. Schuster, F. Weitzer, R. Schmid-Fetzer, M. Ohno, H. Xu, Z.K. Liu, S. Shang, W. Zhang, Reassessment of the Al-Mn system and a thermodynamic description of the Al-Mg-Mn system, Zeitschrift Fuer Met. Res. Adv. Tech. 98 (2007) 855–871.

[38] Y.P. Ren, G.W. Qin, W.L. Pei, H.D. Zhao, Y. Guo, H.X. Li, M. Jiang, S.M. Hao, Isothermal section of the Mg-Al-Mn ternary system at 400 °C, J. Alloys Compd. 479 (2009) 237–241.

[39] M. Ohno, D. Mirkovic, R. Schmid-Fetzer, Liquidus and solidus temperatures of Mg-rich Mg-Al-Mn-Zn alloys, Acta Mater. 54 (2006) 3883–3891.

[40] W. Zhou, N.N. Aung, A. Choudhary, M. Kanouni, Evaluation of corrosion resistance of magnesium alloys in radiator coolants, Corros. Eng. Sci. Technol. 46 (2011) 386–391.

[41] Z. Yu, M. Hu, A. Tang, M. Wu, J. He, Z. Gao, F. Wang, C. Li, B. Chen, J. Liu, Effect of aluminium on the microstructure and mechanical properties of as-cast magnesium–

manganese alloys, Mater. Sci. Technol. 33 (2017) 2086–2096.

[42] L. Zhang, Z. Wu, J.H. Wang, Characterization of Al-Mn particles in Mg-6Al-xMn magnesium alloys, in: Mater. Sci. Eng. Proc. 3rd Annu. 2015 Int. Conf. Mater. Sci. Eng. (ICMSE2015, Guangzhou, Guangdong, China, 15-17 May 2015), CRC Press, 2016: p. 23.

[43] F. Pan, Z. Feng, X. Zhang, A. Tang, The types and distribution characterization of Al-Mn phases in the AZ61 magnesium alloy, in: Procedia Eng., Elsevier Ltd, 2012: pp. 833–839.

[44] O. Lunder, K. Nisancioglu, R.S. Hansen, Corrosion of Die Cast Magnesium-Aluminum Alloys, in: SAE Tech. Pap., 1993: pp. 117–126.

[45] L.-Y. Wei, H. Westengen, T.K. Aune, D. Albright, Characterisation of Manganese-Containing Intermetallic Particles and Corrosion Behaviour of Die Cast Mg-Al-Based Alloys, in: Magnes. Technol. 2000, John Wiley & Sons, Inc., Hoboken, NJ, USA, NJ, USA, 2013: pp. 153–160.

[46] A. Kontio, E.D. Stevens, P. Coppens, R.D. Brown, A.E. Dwight, J.M. Williams, New investigation of the structure of Mn4Al11, Acta Crystallogr. Sect. B Struct. Crystallogr. Cryst. Chem. 36 (1980) 435–436.

[47] S. Thimmaiah, Z. Tener, T.N. Lamichhane, P.C. Canfield, G.J. Miller, Crystal structure, homogeneity range and electronic structure of rhombohedral γ-Mn5Al8, Zeitschrift Fur Krist. - Cryst. Mater. 232 (2017) 601–610.

[48] M. Ellner, The structure of the high-temperature phase MnAl(h) and the displacive transformation from MnAl(h) into Mn_5Al_8, Metall. Trans. A. 21 (1990) 1669–1672.

[49] K. Yoshida, T. Yamamoto, S. Nagata, Microstructure m mnal(R) alloy phase, Jpn. J. Appl. Phys. 13 (1974) 400–410.

[50] K. Yoshida, S. Nagata, On the crystal structure of mnal(R)phase, Jpn. J. Appl. Phys. 10 (1971) 7–10.

[51] B.L. Bramfitt, The effect of carbide and nitride additions on the heterogeneous nucleation behavior of liquid iron, Metall. Trans. 1 (1970) 1987–1995.

[52] H. Arnold, Transformations of the coordinate system (unit-cell transformations), in: Int. Tables Crystallogr., International Union of Crystallography, 2006: pp. 78–85.

[53] JMatPro v. 7.0, (2013).

[54] J.H. Sharp, G.W. Brindley, B.N.N. Achar, Numerical Data for Some Commonly Used Solid State Reaction Equations, J. Am. Ceram. Soc. 49 (1966) 379–382.

[55] S.S. Tamhankar, L.K. Doraiswamy, Analysis of solid-solid reactions: A review, AIChE J. 25 (1979) 561–582.

[56] J. Jach, The thermal decomposition of NaBrO3 part I-Unirradiated material, J. Phys. Chem. Solids. 24 (1963) 63–73.

[57] A.M. Ginstling, B.I. Brounshtein, Concerning the diffusion kinetics of reactions in spherical particles, J. Appl. Chem. USSR. 23 (1950) 1327–1338.

[58] G. Valensi, Kinetics of the oxidation of metallic spherules and powders, Compt. Rend. 202 (1936) 309–312.

[59] R.E. Carter, Kinetic model for solid-state reactions, J. Chem. Phys. 34 (1961) 2010–2015.

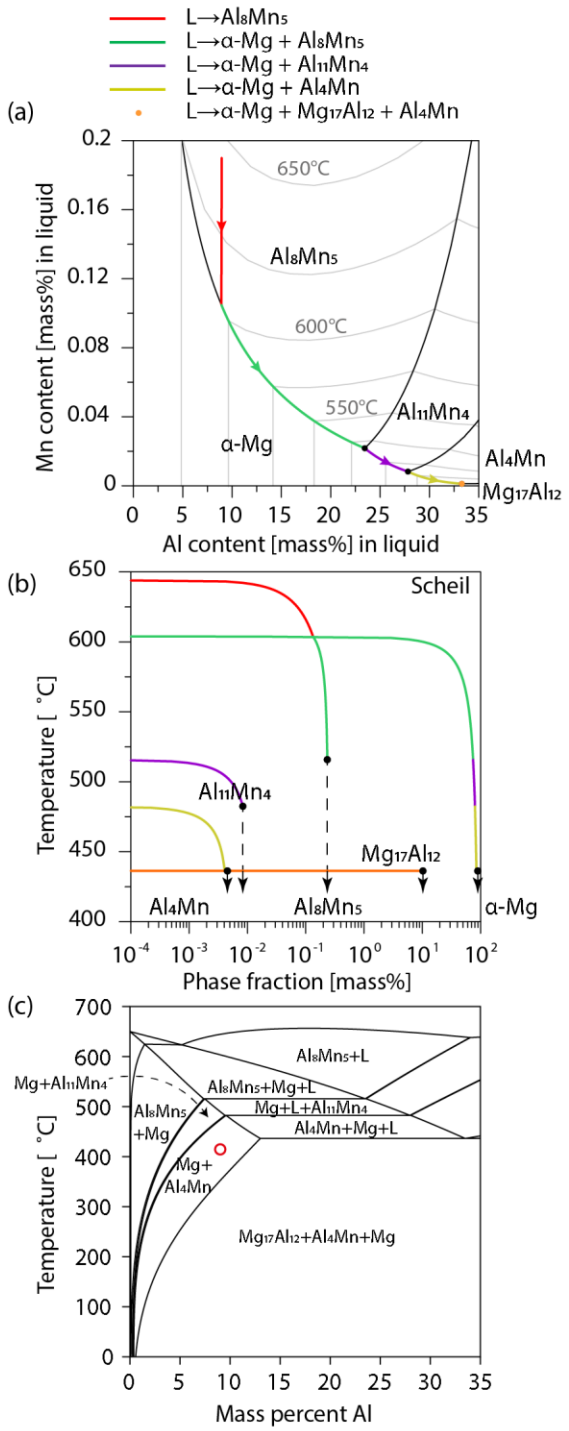

Fig. 1. (a) Mg-Al-Mn liquidus projection and liquid path during Scheil solidification of Mg-9Al-0.19Mn. (b) Development of solid phases on cooling for Scheil conditions. Note the log scale. (c) (99.81-x)Mg-0.19Mn-xAl isopleth. Equilibrated Mg-9Al-0.19Mn at 410 °C is marked by a red circle. Plotted using the Thermo-Calc TCMG4.0 database.

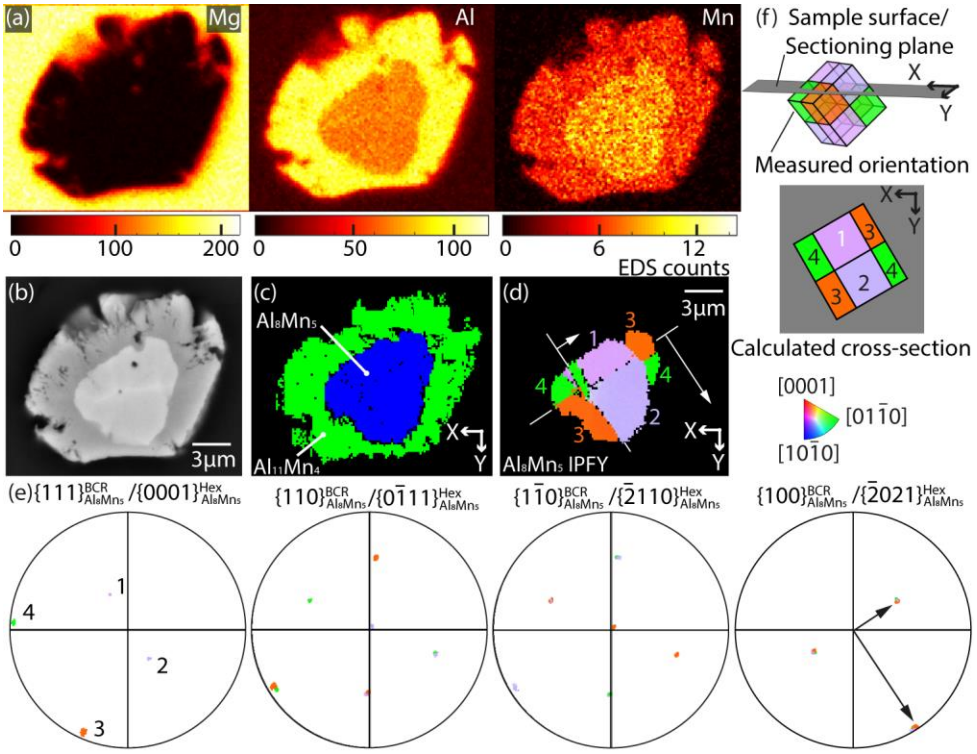

Fig. 2. Typical $Al_{11}Mn_4$-Al_8Mn_5 two-phase particle after 3 days at 410 °C. (a) EDS map showing the shell is richer in Al than the core. (b) BSE image of the particle. (c) EBSD phase map (d) IPF-Y map of the Al_8Mn_5 core showing cyclic twinning. Arrows mark twin interface-normals in the cross section. (e) Al_8Mn_5 pole figures containing four unique $\{111\}_{BCR}$ poles, sharing common {110} or $\{1\text{-}10\}_{BCR}$ planes. Arrows in (d) and (e) show the twin interfaces are $\{100\}_{BCR}$. (f) 3D geometric model of cyclic twinned BCR unit cells and a sectioning plane based on the EBSD measurements (upper) and calculated digital cross-section (lower).

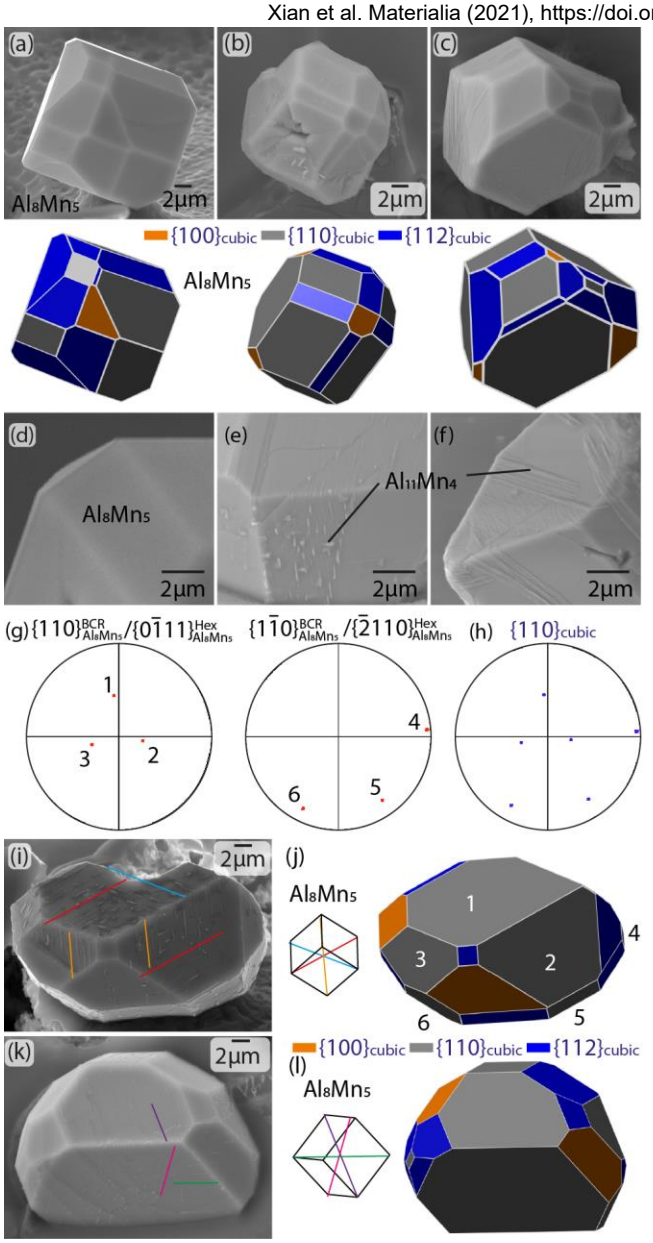

Fig. 3. $Al_{11}Mn_4$ on polyhedral Al_8Mn_5 after solidification at faster cooling rate. Geometric growth models of Al_8Mn_5 are based on {100}, {110}, {112} facets with pseudo-cubic symmetry. (a,d) No trace of $Al_{11}Mn_4$ found, (b,e) $Al_{11}Mn_4$ islands on Al_8Mn_5, (c,f) $Al_{11}Mn_4$ ropes covering Al_8Mn_5. (g) Al_8Mn_5 pole figures from one orientation of the cyclic-twinned BCR-Al_8Mn_5 particle in (i). (h) Pseudo-cubic $\{110\}_{cubic}$ pole figure after merging $\{110\}_{BCR}$ and $\{1\text{-}10\}_{BCR}$ in (g). (i,k) SE images of two Al_8Mn_5 particles with lines of $Al_{11}Mn_4$ marked by coloured vectors. (j,l) BCR-Al_8Mn_5 unit cells superimposed by the coloured vectors showing the lines of $Al_{11}Mn_4$ are parallel with the $<111>_{cubic}$.

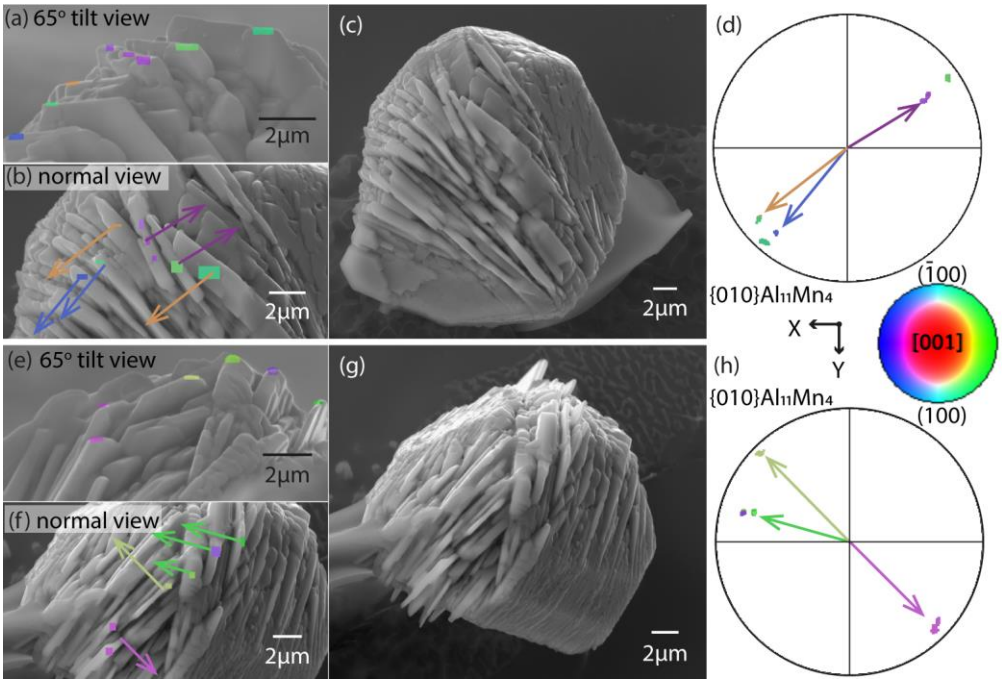

Fig. 4. Two examples of $Al_{11}Mn_4$ plates surrounding Al_8Mn_5 after solidification at slower cooling rate. (a,e) Raw EBSD measurements (IPF-Y) at a tilt angle of 65°. (b,f) Normal view of the same area (0° tilt). Arrows mark $Al_{11}Mn_4$ plate normals. (c,g) Al_8Mn_5 particles fully covered by $Al_{11}Mn_4$. (d,h) The marked arrows ($Al_{11}Mn_4$ plate normals in (b,f)) superimposed on the $\{010\}_{Al11Mn4}$ poles.

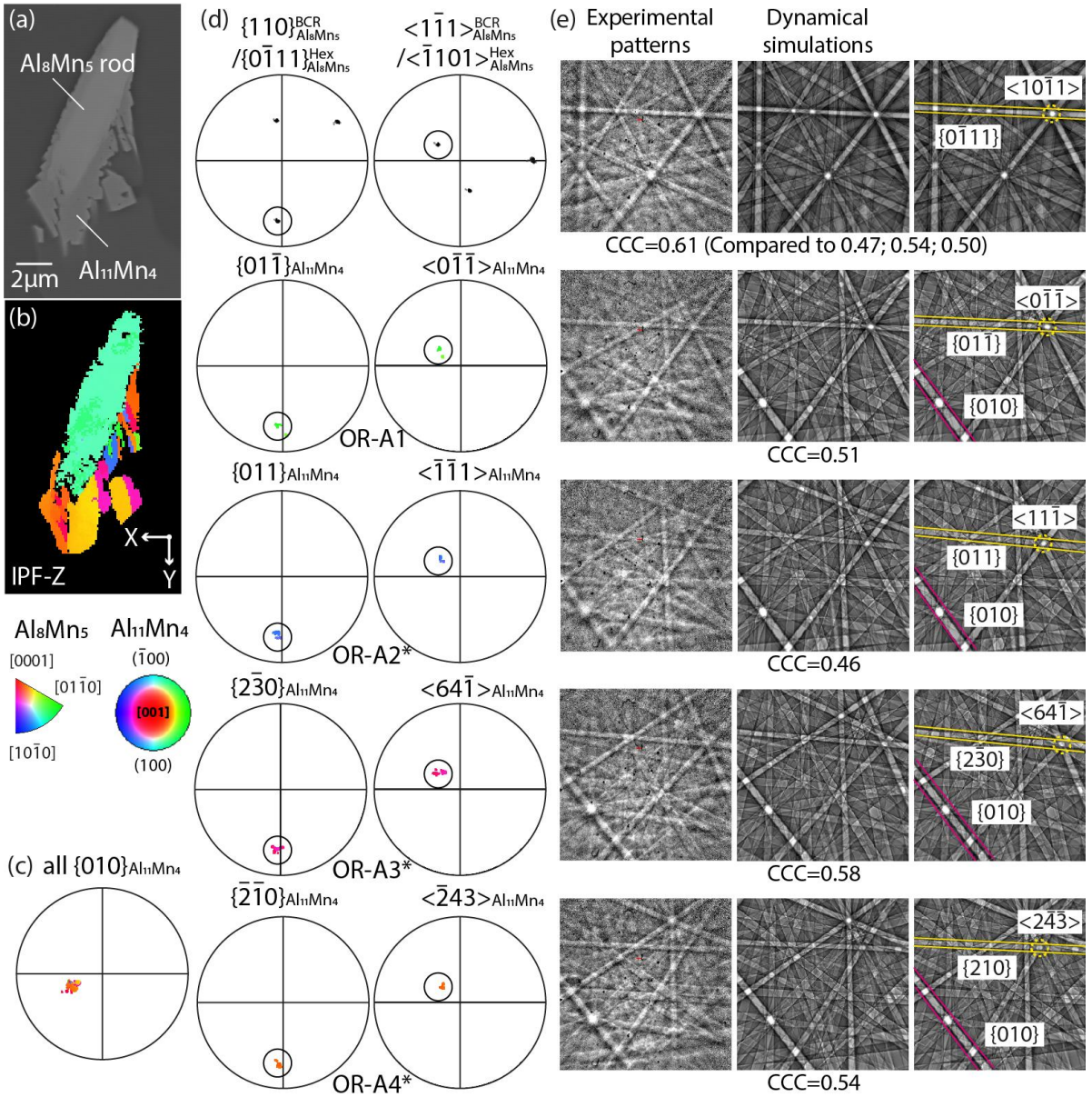

Fig. 5. (a) Cross-section of Al_8Mn_5 rod crystal covered by plates of $Al_{11}Mn_4$. (b) EBSD IPF-Z map of Al_8Mn_5 and $Al_{11}Mn_4$. (c) Pole figures of the main growth facets {010} of $Al_{11}Mn_4$. (d) Selected pole figures of Al_8Mn_5 and $Al_{11}Mn_4$ shows four orientation relationships of $Al_{11}Mn_4$ plates on the single crystal Al_8Mn_5 rod. (e) Cross correlation coefficients (CCC) of experimental patterns and dynamical simulations. N.B. any mis-indexed $Al_{11}Mn_4$ orientations have CCC values smaller than 0.2.

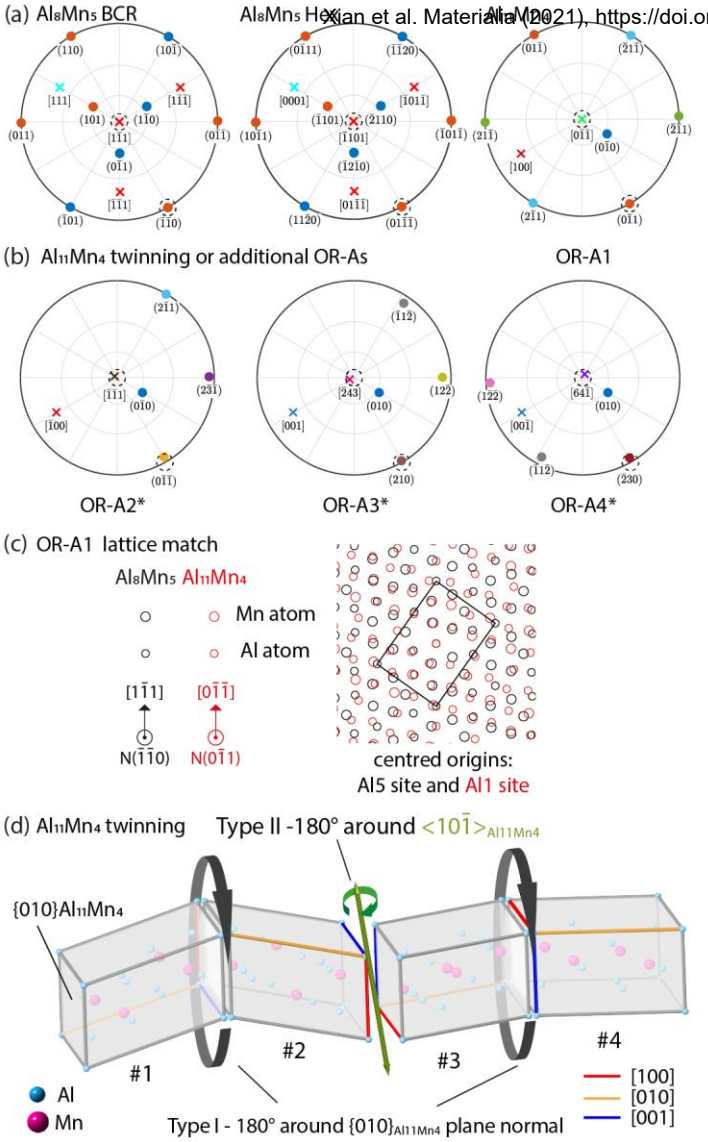

Fig. 6. Orientation relationships OR-As between $Al_{11}Mn_4$ and Al_8Mn_5, and their correlation with self-twinned $Al_{11}Mn_4$ orientations. (a) Stereographic projections centred on $[1\bar{1}1]_{Al8Mn5\_BCR}$//$[0\bar{1}\bar{1}]_{Al11Mn4}$ parallel planes $(\bar{1}\bar{1}0)_{Al8Mn5}$//$(0\bar{1}1)_{Al11Mn4}$ for OR-A1. •=planes, × =directions. (b) Three $Al_{11}Mn_4$ stereographic projections share more possible ORs (A2*,A3*,A4*) with the Al_8Mn_5 nuclei as measured in Fig. 5(d), which are also twinned from the $Al_{11}Mn_4$ orientation in OR-A1. (c) Planar atomic lattice matching of OR-A1 between the $(\bar{1}\bar{1}0)_{Al8Mn5}$ and $(0\bar{1}1)_{Al11Mn4}$ planes, with $[1\bar{1}1]_{Al8Mn5\_BCR}$ and $[0\bar{1}\bar{1}]_{Al11Mn4}$ directions pointing up. (d) Two types of $Al_{11}Mn_4$ twinning operations: i) rotating 180° in $\{010\}_{Al11Mn4}$, ii) rotating 180° along $\langle 10\bar{1}\rangle_{Al11Mn4}$. Note that the four $Al_{11}Mn_4$ orientations share common {010} planes and parallel <100> or <001> directions, same as the $Al_{11}Mn_4$ stereograms in (a-b).

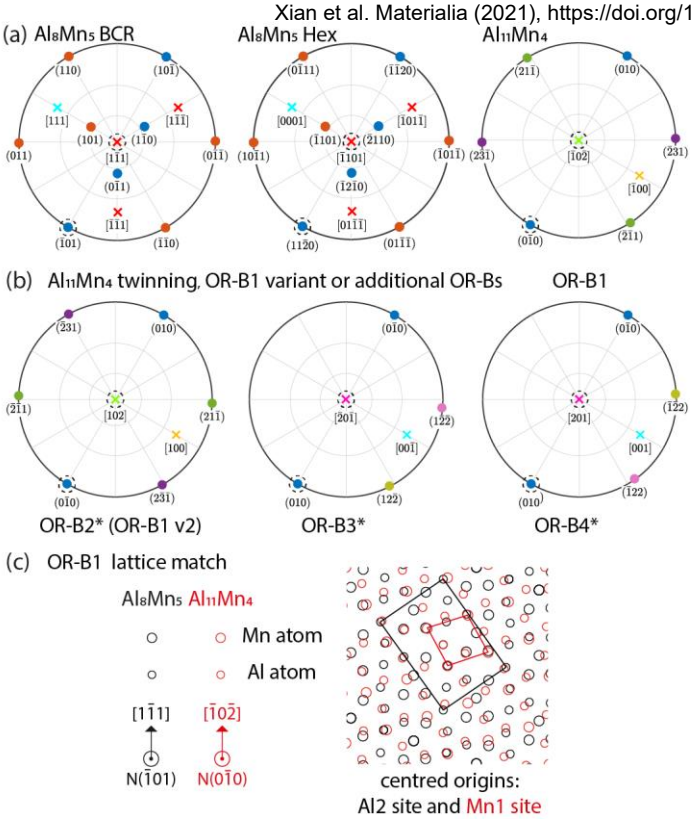

Fig. 7. Orientation relationships OR-Bs between $Al_{11}Mn_4$ and Al_8Mn_5, and their correlation with self-twinned $Al_{11}Mn_4$ orientations. (a) Stereographic projections centred on $[1\bar{1}1]_{Al8Mn5\_BCR}//[\bar{1}0\bar{2}]_{Al11Mn4}$ parallel planes $(\bar{1}01)_{Al8Mn5}//(0\bar{1}0)_{Al11Mn4}$ for OR-B1. •=planes, × =directions. (b) Three $Al_{11}Mn_4$ stereographic projections share more possible ORs (B2*,B3*,B4*) with the Al_8Mn_5 nuclei, which are also twinned from the $Al_{11}Mn_4$ orientation in OR-B1. (c) Planar atomic lattice matching of OR-B1 between the $(\bar{1}01)_{Al8Mn5}$ and $(0\bar{1}0)_{Al11Mn4}$ planes, with $[1\bar{1}1]_{Al8Mn5\_BCR}$ and $[\bar{1}0\bar{2}]_{Al11Mn4}$ directions pointing up.

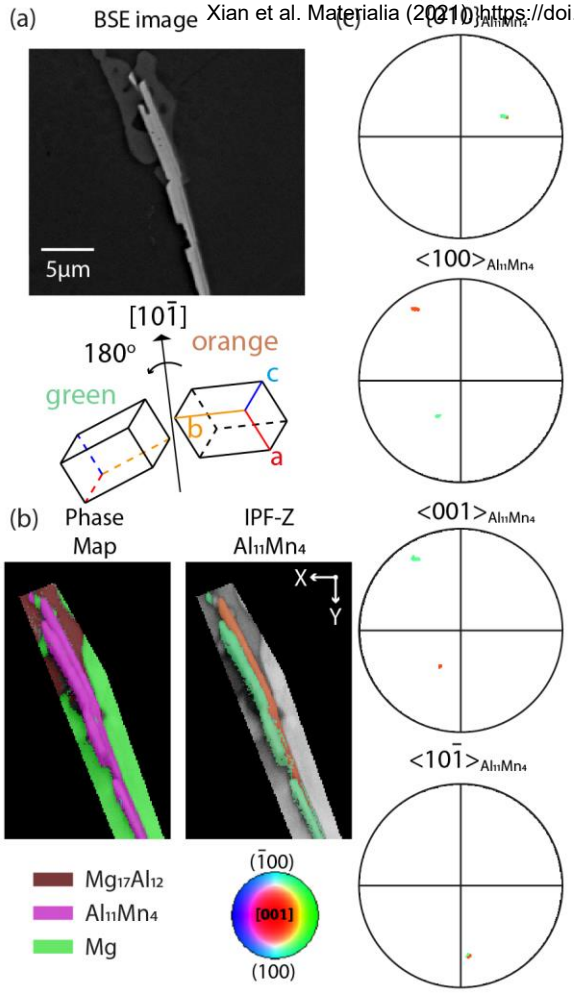

Fig. 8. Twinned $Al_{11}Mn_4$ plates after solidification. (a) BSE image and unit cells of the $Al_{11}Mn_4$ twinned OR. (b) Phase map and EBSD IPFZ map of two $Al_{11}Mn_4$ twins. (c) Pole figures showing common planes {010} and directions $\langle 10\bar{1} \rangle_{Al11Mn4}$. <100> and <001> are swapped by the twinning operation type II.

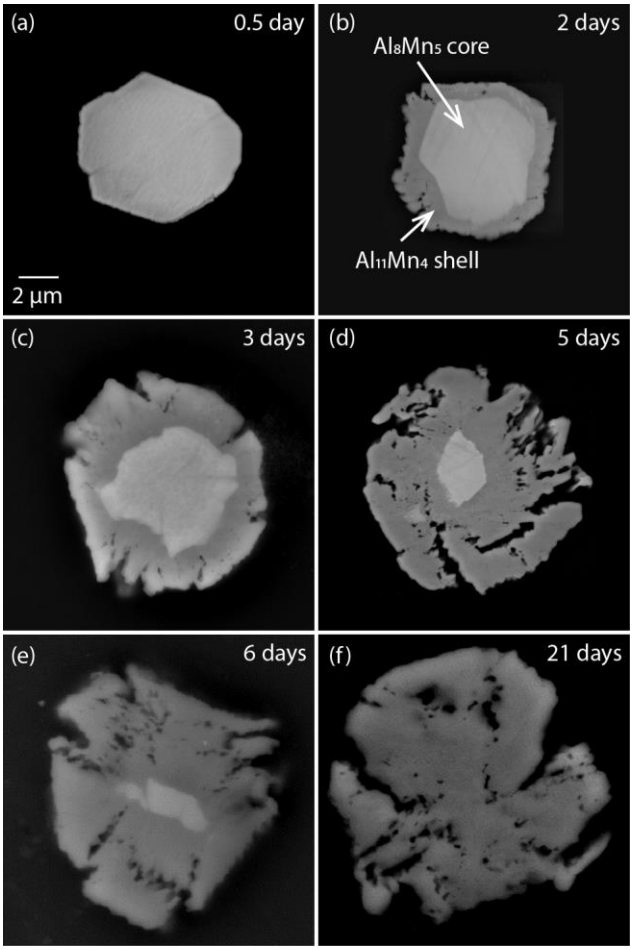

Figure 9: Typical BSE images of cross-sections through Al_8Mn_5-$Al_{11}Mn_4$ core-shell particles at six times during solid-state transformation at 410 °C. α-Mg appears black.

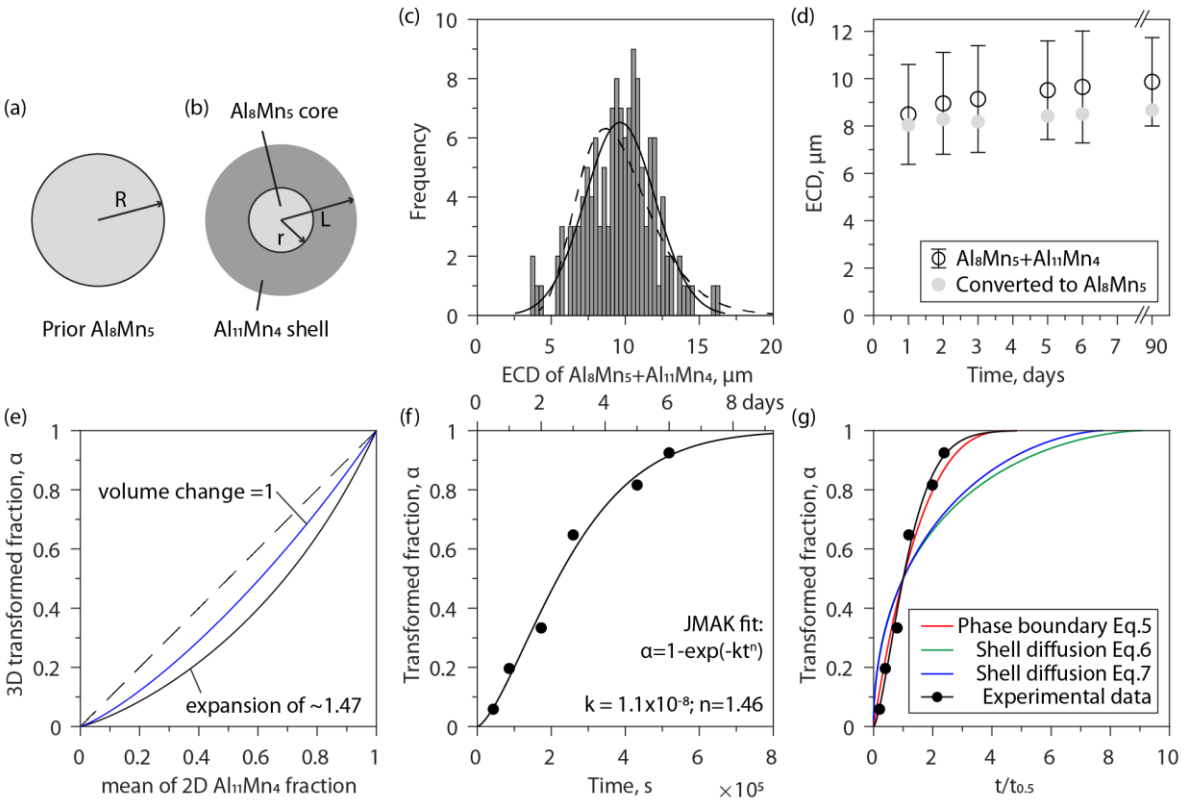

Fig. 10. (a-b) Schematic showing a prior Al_8Mn_5 particle in (a) and partly transformed particle with a $Al_{11}Mn_4$ shell in (b). (c) The ECD distribution of Al_8Mn_5+$Al_{11}Mn_4$ particles after 6 days ageing, and its normal (solid line) and lognormal (dashed line) distribution fit curves. (d) The mean ECDs of Al_8Mn_5+$Al_{11}Mn_4$ (2L) particles and converted sizes (2R) of prior Al_8Mn_5 after different aging times. (e) Relationships between calculated 3D transformed fraction vs. mean of measured 2D $Al_{11}Mn_4$ fraction, with and without a volume change. (f) Experimental data (i.e. calculated α with expansion considered) vs. time, fitted by JMAK equation. (g) Comparison between the experimental data and the kinetic models in Eq. 5-7 plotted against reduced time, $t_{0.5}$ = time for 50% transformation.

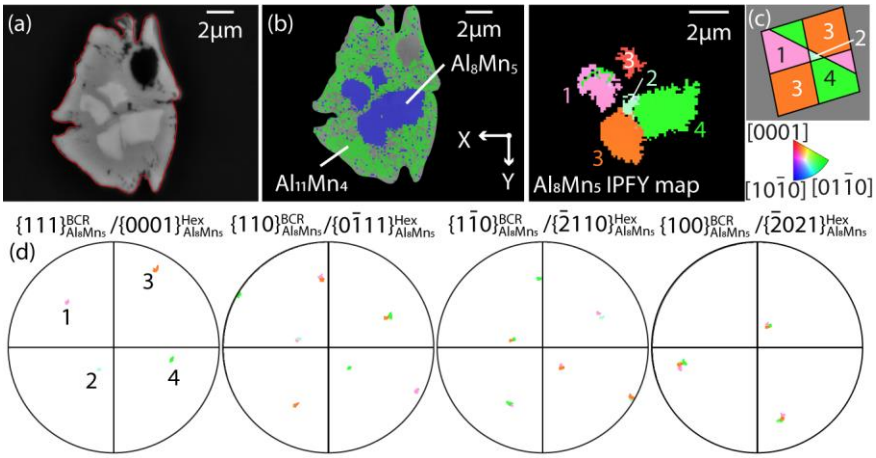

Fig. 11. Faster transformation along Al_8Mn_5 twin interfaces. (a) BSE image of Al_8Mn_5 transforming into $Al_{11}Mn_4$ after 3 days at 410°C and the black region within the core-shell particle in (a) is α-Mg. (b) EBSD phase map and IPFY map of Al_8Mn_5. (c) Calculated cross-section assuming a cyclic twin with {100} twin planes. (d) Pole figures of four twinned Al_8Mn_5 orientations.

Table 1. Summary of EDS analysis of the two Al-Mn IMCs.

	Al [at%]	Mn [at %]	Mg [at%]
Al_8Mn_5	55	45	—
$Al_{11}Mn_4$	68	31	1

Table 2 Crystal structures of Al_8Mn_5 and $Al_{11}Mn_4$. [46,48]

	Space group	Unit cell setting	Lattice parameters [Å , °]						Ref
			a	B	c	α	β	γ	
Al_8Mn_5	R3m	hexagonal	12.667	12.667	7.942	90	90	120	[48]
		primitive rhombohedral	7.778	7.778	7.778	109.04	109.04	109.04	
		body centred rhombohedral	9.029	9.029	9.029	89.09	89.09	89.09	
$Al_{11}Mn_4$	P-1	—	5.095	8.879	5.051	89.35	100.47	105.08	[46]

Table 3. A summary of variants of OR-A1 and OR-B1.

		Parallel planes			Parallel directions		
		BCR-Al_8Mn_5	Hex-Al_8Mn_5	$Al_{11}Mn_4$	BCR-Al_8Mn_5	Hex-Al_8Mn_5	$Al_{11}Mn_4$
OR-A1	v1	(110)	$(0\bar{1}11)$	$(01\bar{1})$	$[1\bar{1}1]$	$[\bar{1}101]$	$[0\bar{1}\bar{1}]$
	v2	$(\bar{1}\bar{1}0)$	$(01\bar{1}\bar{1})$	$(01\bar{1})$	$[\bar{1}1\bar{1}]$	$[1\bar{1}0\bar{1}]$	$[0\bar{1}\bar{1}]$
	v3	(101)	$(\bar{1}101)$	$(01\bar{1})$	$[\bar{1}11]$	$[10\bar{1}1]$	$[0\bar{1}\bar{1}]$
	v4	$(\bar{1}0\bar{1})$	$(1\bar{1}0\bar{1})$	$(01\bar{1})$	$[1\bar{1}\bar{1}]$	$[\bar{1}01\bar{1}]$	$[0\bar{1}\bar{1}]$
	v5	(011)	$(10\bar{1}1)$	$(01\bar{1})$	$[11\bar{1}]$	$[0\bar{1}11]$	$[0\bar{1}\bar{1}]$
	v6	$(0\bar{1}\bar{1})$	$(\bar{1}01\bar{1})$	$(01\bar{1})$	$[\bar{1}\bar{1}1]$	$[01\bar{1}\bar{1}]$	$[0\bar{1}\bar{1}]$
OR-B1	v1	$(\bar{1}01)$	$(11\bar{2}0)$	$(0\bar{1}0)$	$[1\bar{1}1]$	$[\bar{1}101]$	$[\bar{1}0\bar{2}]$
	v2	$(\bar{1}01)$	$(11\bar{2}0)$	$(0\bar{1}0)$	$[\bar{1}1\bar{1}]$	$[1\bar{1}0\bar{1}]$	$[\bar{1}0\bar{2}]$
	v3	$(01\bar{1})$	$(1\bar{2}10)$	$(0\bar{1}0)$	$[\bar{1}11]$	$[10\bar{1}1]$	$[\bar{1}0\bar{2}]$
	v4	$(01\bar{1})$	$(1\bar{2}10)$	$(0\bar{1}0)$	$[1\bar{1}\bar{1}]$	$[\bar{1}01\bar{1}]$	$[\bar{1}0\bar{2}]$
	v5	$(1\bar{1}0)$	$(\bar{2}110)$	$(0\bar{1}0)$	$[11\bar{1}]$	$[0\bar{1}11]$	$[\bar{1}0\bar{2}]$
	v6	$(1\bar{1}0)$	$(\bar{2}110)$	$(0\bar{1}0)$	$[\bar{1}\bar{1}1]$	$[01\bar{1}\bar{1}]$	$[\bar{1}0\bar{2}]$

*Table 4: Compositions and fractions of phases before and after solid state transformation at 410℃ using Eq. 3, assuming zero solubility of Mn in α-Mg, a bulk alloy composition of Mg-8.95Al-0.19Mn (mass%), and stoichiometric IMCs. * = calculated for 1 mol of alloy.*

	phase	composition [mol fraction]			fraction	fraction	density	fraction	volume*
		Mg	Al	Mn	[by mol]	[by mass]	[g/cm³]	[by vol]	[cm³]
before	Al_8Mn_5	0	0.6154	0.3846	0.0022	0.0034	4.43	0.0014	0.0188
	α-Mg	0.9198	0.0802	0	0.9978	0.9966	1.80	0.9986	13.6200
after	$Al_{11}Mn_4$	0	0.7333	0.2667	0.0032	0.0045	3.96	0.0020	0.0277
	α-Mg	0.9207	0.0793	0	0.9968	0.9955	1.80	0.9980	13.6103

SUPPLEMENTARY INFORMATION

$Al_{11}Mn_4$ formation on Al_8Mn_5 during the solidification and heat treatment of AZ-series magnesium alloys

J.W. Xian[1,*], L. Peng[1], G. Zeng[2], D. Wang[1], C.M. Gourlay[1,*]

[1] Department of Materials, Imperial College London. SW7 2AZ. UK
[2] School of Materials Science and Engineering, Central South University, Changsha, 410083, China

SI-section 1. Extended Methods

For cross-sectional EBSD, conventional metallography preparation techniques are used, noting that ethanol is used instead of water throughout grinding and polishing for better surface finish of Mg alloy.

For EBSD on 3D particles, samples are polished followed by chemical etching. In order to correctly link the coordinates of SEM imaging and EBSD measurements (normally taken at ~70° tilt), we used two similar mapping methods:

Method 1 was used for Fig. 4, unlike the cross-sectional EBSD analysis, we need to (a) first target on tilted 3D crystals that can generate good Kikuchi patterns, and carry out EBSD calibrations as normal; (b) then after EBSD mapping, tilt 3D crystals (SEM stage) back to 0° for an undistorted SEM imaging. Then the SEM imaging and 3D crystals are correctly linked together, i.e. the orientations measured is with reference to the 0°-tilt 3D crystal.

Method 2 was used for SI-Fig. 4, (a) first, one can tilt the SEM stage (i.e. 3D crystals) at any angle between ~50° and 70° to obtain good Kikuchi patterns, and take a SEM image at the same tilt angle. (b) Secondly, to set up the EBSD mapping, one needs to tell EBSD software (calibration) that the sample stage was at 0° tilt. This is counter-intuitive, but it is geometrically and mathematically valid for the EBSD software to give you the correct orientation with reference to the SEM image taken at the tilt angle. The orientations measured here are with reference to tilted 3D crystal (i.e. the fixed beam view).

SI-Fig.1 and 2 show examples of using dynamical simulated EBSD patterns within Bruker DynamicS to deduce the best fitting orientation and phase.

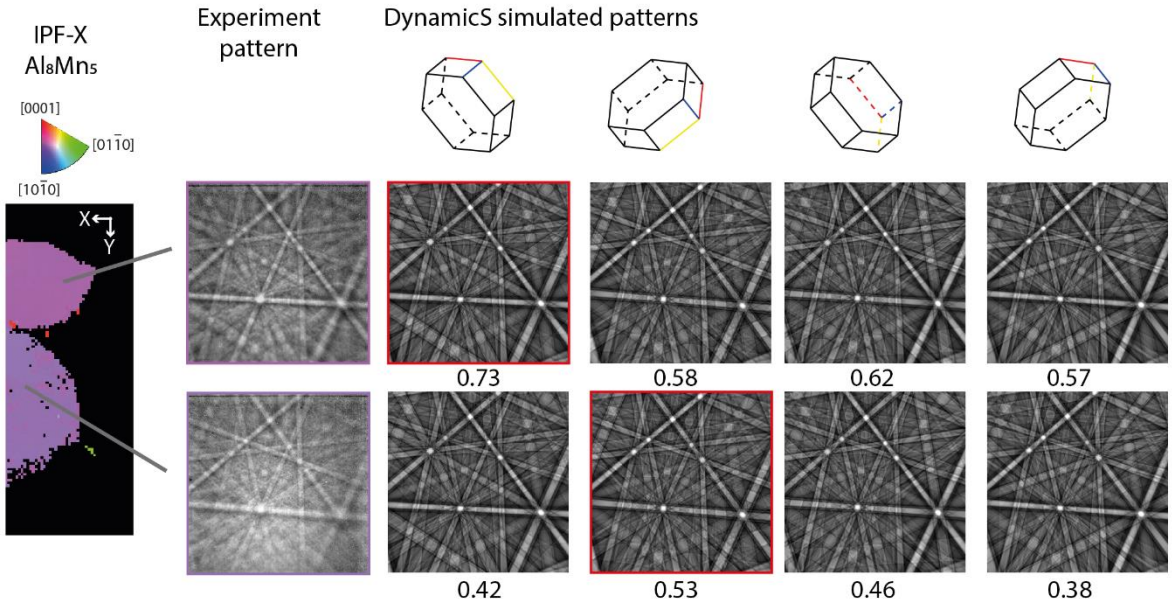

SI-Fig. 1 Two Al_8Mn_5 orientations (twinned from each other) are checked by dynamical simulations, for the top Al_8Mn_5 the first simulated pattern (CCC = 0.73 in red box) is the best solution; for the bottom Al_8Mn_5 the second simulated pattern has the highest CCC=0.53 (in red box) among all four possible orientations in cyclically twinned Al_8Mn_5. This confirms the EBSD is accurate to distinguish R3mH Al_8Mn_5 orientations.

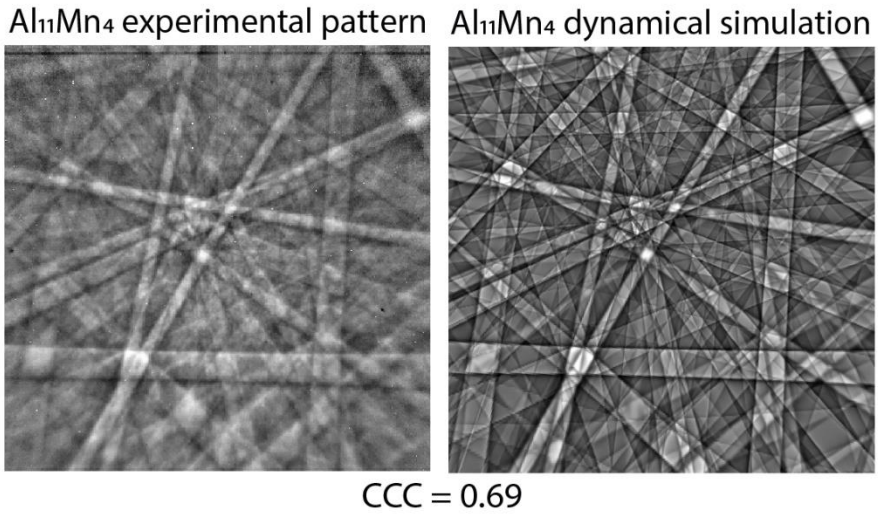

SI-Fig. 2 Cross correlation coefficient (CCC) between a $Al_{11}Mn_4$ experimental pattern and its dynamical simulation pattern can be as good as 0.69, confirming $Al_{11}Mn_4$ is the correct phase and suitable for EBSD.

SI-section 2. Low magnification microstructures from AZ31 and AZ91 at each cooling rate

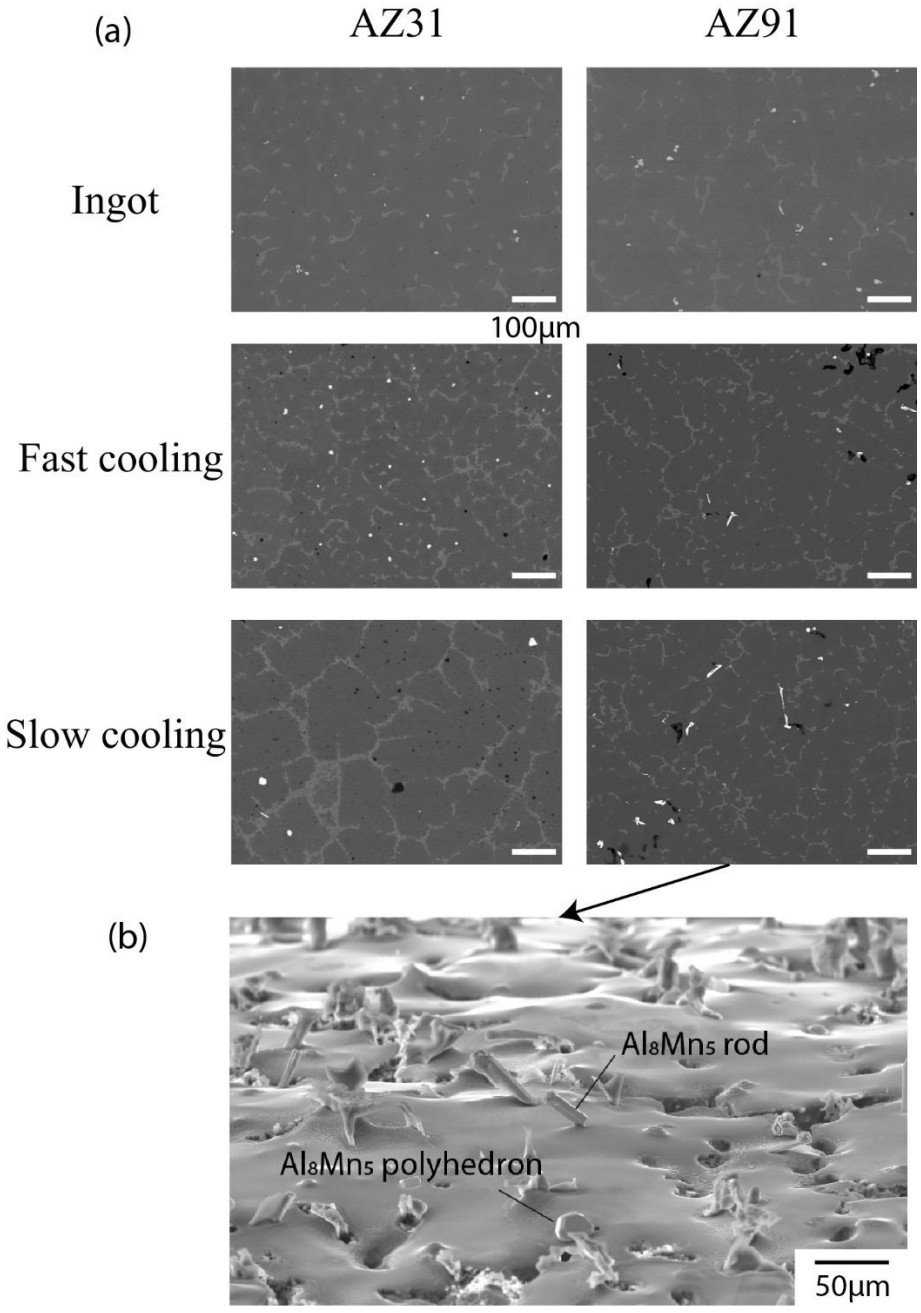

SI-Fig. 3 (a) BSE images of overall microstructures for different cooling conditions in AZ31 and AZ91. (b) Deep-etched slow-cooled AZ91 sample showing both Al_8Mn_5 polyhedral particles and rods.

SI-section 3. Growth crystallography of Al_8Mn_5 rod and phase identification

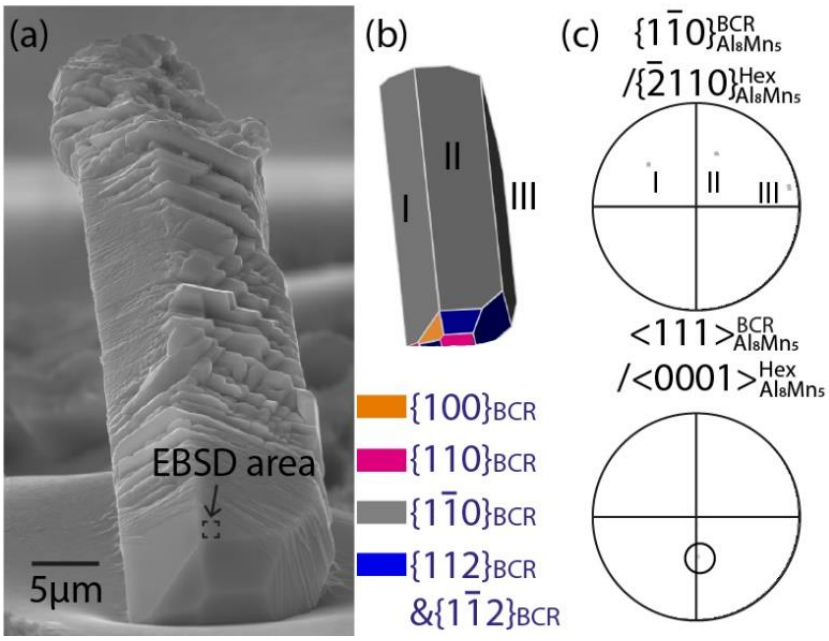

SI-Fig. 4 (a) Al_8Mn_5 rod crystal partially covered by parallel plates of $Al_{11}Mn_4$, (b) Al_8Mn_5 geometrical facet model, (c) selected Al_8Mn_5 pole figures in the BCR and hexagonal settings, showing the major growth facets $\{1\text{-}10\}_{BCR}$ and growth direction $<111>_{BCR}$ of the single crystal Al_8Mn_5 rod.

SI-section 4. Orientation relationships

SI-Table. 1 The $Al_{11}Mn_4$ planes involved in OR-As and OR-Bs are the first 11 planes in the reflector list generated in Bruker Esprit 2.1, with 6 $Al_{11}Mn_4$ planes in either OR-As or OR-Bs see SI-Fig. 3 and with $\{010\}_{Al11Mn4}$ common to both ORs. The reflector list is ranked by band intensity and structure factor.

No	HKL	d_{HKL}	I	$\|F\|_{HKL}$	$I_{Rel.}$	Mult	☑
1	0 4 0	2.142	11.7	25.3	100.0	2	
2	-2 -1 1	2.141	11.0	23.8	94.0	2	
3	2 -1 1	2.089	10.5	22.7	89.8	2	
4	0 -2 2	2.183	10.5	22.7	89.6	2	
5	-1 2 2	2.179	10.3	22.3	88.0	2	
6	2 -3 0	2.143	10.0	21.7	85.7	2	
7	2 1 0	2.182	9.3	20.1	79.4	2	
8	0 2 2	2.113	9.2	19.9	78.5	2	
9	-2 3 1	2.073	9.0	19.5	77.2	2	
10	1 -1 2	2.070	8.7	18.9	74.6	2	
11	-1 -2 2	2.012	7.7	16.7	66.1	2	
12	-4 2 1	1.270	7.5	16.3	64.2	2	
13	-1 0 4	1.259	7.4	16.0	63.4	2	
14	-2 1 2	1.948	7.0	15.1	59.8	2	
15	-3 1 3	1.299	6.9	14.9	59.0	2	
16	-2 -5 1	1.251	6.8	14.7	58.1	2	
17	-1 6 2	1.280	6.7	14.4	57.0	2	
18	1 3 1	1.943	6.3	13.7	54.3	2	
19	1 3 0	2.217	6.2	13.3	52.7	2	

Total reflector number: 138 (276) ☑ Special reflectors

Lower limits 23.30 I_{min}

0.50 d_{min}

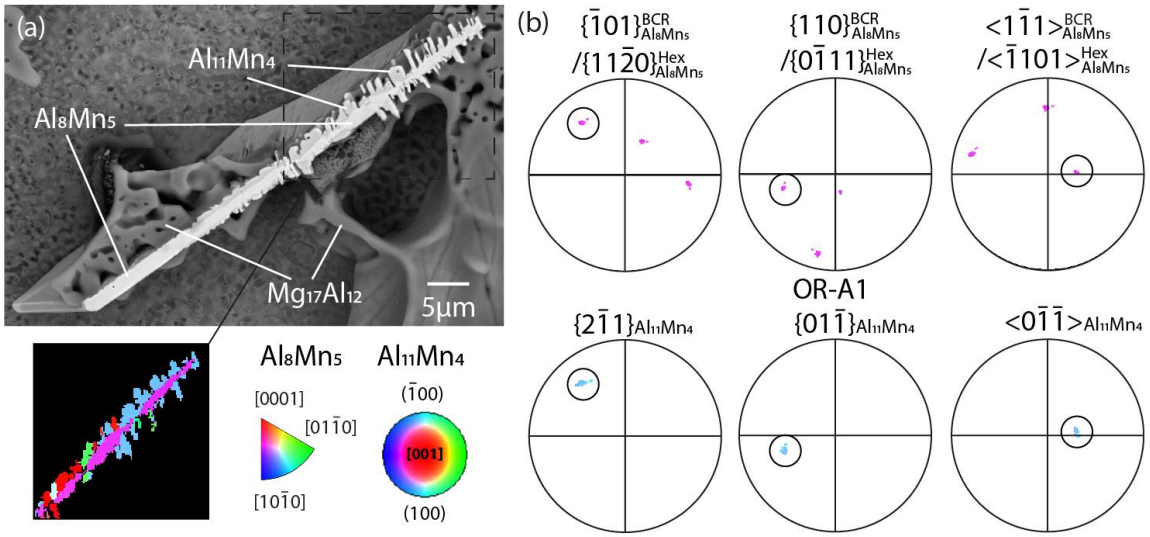

SI-Fig. 5 EBSD measurement of OR-A1 between the Al_8Mn_5 and $Al_{11}Mn_4$ in slow-cooled AZ31. (a) SE image of etched Al_8Mn_5 with surrounding $Al_{11}Mn_4$ and $Mg_{17}Al_{12}$, and IPF-Y map of Al_8Mn_5 and all $Al_{11}Mn_4$ particles, showing the majority blue $Al_{11}Mn_4$ orientation sharing OR-A1 with Al_8Mn_5. (b) Pole figures of typical parallelisms involved in OR-A1. All four $Al_{11}Mn_4$ orientations of OR-As can be found in this sample.

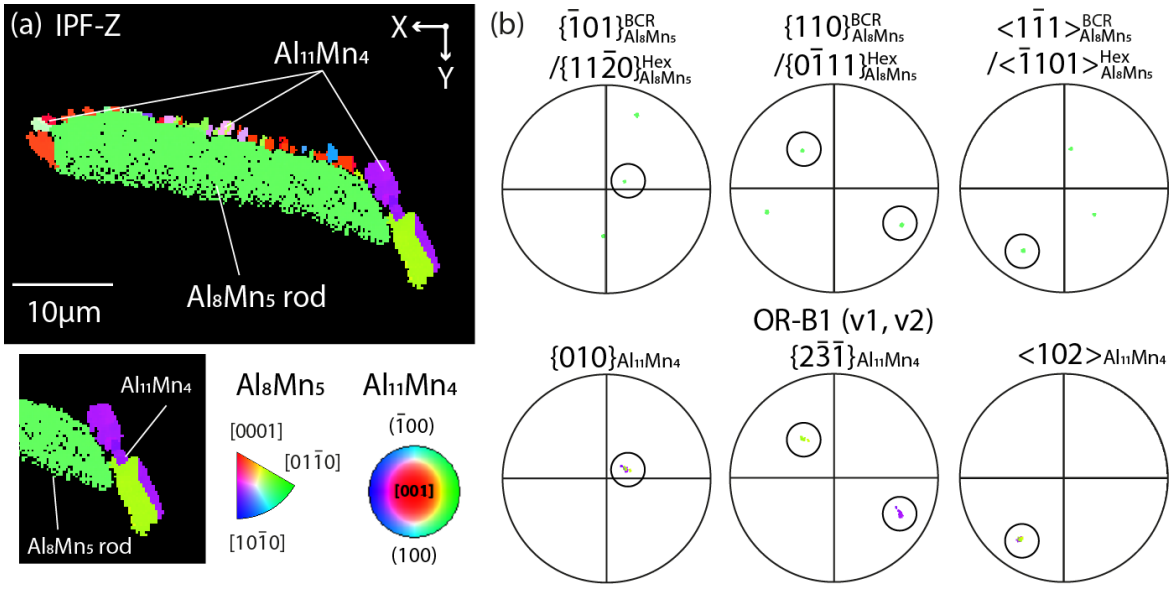

SI-Fig. 6 EBSD measurement of two variants of OR-B1 between the single crystal Al_8Mn_5 rod and $Al_{11}Mn_4$ shell in AZ91. (a) IPF-Z map of Al_8Mn_5 and all $Al_{11}Mn_4$ particles, with the insert showing only the two $Al_{11}Mn_4$ orientations sharing OR-B1 to Al_8Mn_5. (b) Pole figures of typical parallelisms involved in OR-B1, one can refer to Fig. 7 in the main manuscript for reasons behind the choices of planes shown here. Note that $Al_{11}Mn_4$ {010} growth facets are nearly parallel to the cross section (see the $\{010\}_{Al11Mn4}$ pole figure), which is likely to be the interface on its parallel $\{11\text{-}20\}_{Al8Mn5}$ the hexagonal facets as being defined in OR-B1. In other examples, all four $Al_{11}Mn_4$ orientations of OR-Bs are also found together.

SI-section 5. Core-shell transformation : relationship between $\overline{A_A}$ and α

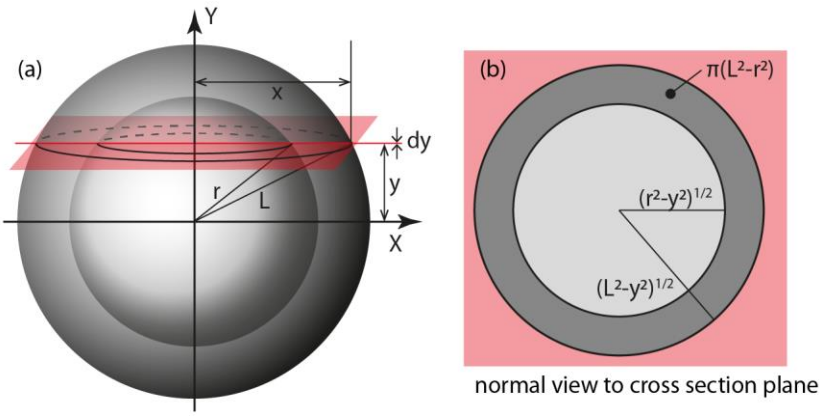

SI-Fig. 7 Schematics showing the geometrical relationship between mean of 2D shell fraction vs. 3D volume fraction.

r radius of core

L radius of core-shell particle

$\overline{A_A}$ mean of 2D shell fractions

V_V volume fraction of the core in core-shell particles, $\left(\frac{r}{L}\right)^3$

SI-Fig. 7(a) is a schematic of a 3D core-shell particle, with a core radius of r and a total radius of L. In SI-Fig. 7(b), a sectioning red plane of infinitessimal thickness, dy, (and y distance from sphere centre) can intersect the whole particle generating 1) a core-shell cross section when $y < r$; or 2) a shell-only cross section when $y \geq r$.

From the experimental 2D images, one can obtain the mean of 2D shell fractions from ~100 particles as $\overline{A_A}$, which can be derived as follows:

When $y < r$, the shell area fraction shown in SI-Fig. 7(b) is:

$$\frac{\pi(L^2 - r^2)}{\pi(L^2 - y^2)} \qquad \text{Eq. 1}$$

By integrating this value from 0 to r, one can get the total of 2D shell fractions as:

$$\int_0^r \frac{\pi(L^2 - r^2)}{\pi(L^2 - y^2)} dy \qquad \text{Eq. 2}$$

Then the mean of 2D shell fractions with a core becomes for $y < r$:

$$\frac{\int_0^r \frac{\pi(L^2 - r^2)}{\pi(L^2 - y^2)} dy}{r} \qquad \text{Eq. 3}$$

When $y \geq r$, the mean of 2D shell fractions without a core is 1.

For isotropic uniform randomness [1], the probability of sectioning through the core is r/L, and that through the shell-only is $(L - r)/L$. Therefore, the effective mean of all 2D shell fractions (with and without a core) becomes:

$$\overline{A_A} = \frac{r}{L} * \frac{\int_0^r \frac{\pi(L^2 - r^2)}{\pi(L^2 - y^2)} dy}{r} + \frac{L - r}{L} * 1 \quad \text{Eq. 4}$$

To assist the understanding of this integral method, one can also assume that there are 1000 uniformly parallel slices in total that section the whole particle.

1) For $y < r$, there are $\frac{r}{L} * 1000$ slices, making a numerical subtotal of 2D shell fractions with a core as: $\frac{r}{L} * 1000 * \frac{\int_0^r \frac{r\pi(L^2-r^2)}{\pi(L^2-y^2)} dy}{r}$.
2) For $y \geq r$, there are $\frac{L-r}{L} * 1000$ slices, making a numerical subtotal of 2D shell fractions without a core as: $\frac{L-r}{L} * 1000 * 1$.

Thus, the numerical mean of total 2D shell fractions is:

$$\frac{\frac{r}{L} * 1000 * \frac{\int_0^r \frac{\pi(L^2 - r^2)}{\pi(L^2 - y^2)} dy}{r} + \frac{L - r}{L} * 1000 * 1}{1000} \quad \text{Eq. 5}$$

Note that the total number of slices 1000 can be cancelled out easily in Eq. 5, making it in the same form as Eq. 4.

The integral for $\overline{A_A}$, i.e. the mean of 2D shell fractions in Eq. 4, is briefly shown below, noting that r and L are independent of y, and are constants for a fixed core-shell particle.

$$\overline{A_A} = \frac{r}{L} * \frac{\int_0^r \frac{r\pi(L^2-r^2)}{\pi(L^2-y^2)} dy}{r} + \frac{L-r}{L} * 1$$

$$\overline{A_A} = 1 - \left\{ \frac{r}{L} - \frac{1}{L} \int_0^r \frac{\pi(L^2-r^2)}{\pi(L^2-y^2)} dy \right\}$$

$$\overline{A_A} = 1 - \left\{ \frac{r}{L} - \frac{L^2-r^2}{L} \int_0^r \frac{1}{L^2-y^2} dy \right\}$$

where $\int_0^r \frac{1}{L^2-y^2} dy = \frac{1}{2L} \int_0^r \left(\frac{1}{L-y} - \frac{1}{L+y} \right) dy$, which resembles a standard integral of $\int \frac{1}{1-x^2} dx$.

Thus, we continue,

$$\overline{A_A} = 1 - \left\{ \frac{r}{L} - \frac{L^2-r^2}{2L^2} \int_0^r \left(\frac{1}{L-y} - \frac{1}{L+y} \right) dy \right\}$$

$$\overline{A_A} = 1 - \left\{ \frac{r}{L} - \frac{L^2-r^2}{2L^2} * |-\ln(L-y) + \ln(L+y)|_0^r \right\}$$

$$\overline{A_A} = 1 - \left\{ \frac{r}{L} - \frac{L^2-r^2}{2L^2} \ln\left(\frac{L+r}{L-r}\right) \right\} \quad \text{Eq. 6}$$

Note that in Eq. 6, parts in curly brackets are the mean of 2D core fractions.

Eq. 6 can be rearranged as:

$$\overline{A_A} = 1 - \left\{ \frac{r}{L} - \frac{1-\left(\frac{r}{L}\right)^2}{2} \ln\left(\frac{1+\frac{r}{L}}{1-\frac{r}{L}}\right) \right\} \quad \text{Eq. 7}$$

The volume fraction of the core is

$$V_V = \left(\frac{r}{L}\right)^3 \quad \text{Eq. 8}$$

So $\frac{r}{L} = V_V^{\frac{1}{3}}$, and substituting into Eq. 7,

$$\overline{A_A} = 1 - \left\{ V_V{}^{\frac{1}{3}} - \frac{1-V_V{}^{\frac{2}{3}}}{2} \ln\left(\frac{1+V_V{}^{\frac{1}{3}}}{1-V_V{}^{\frac{1}{3}}}\right) \right\} \quad \text{Eq. 9}$$

Now we need to consider the volume expansion during the $Al_8Mn_5 \rightarrow Al_{11}Mn_4$ phase transformation, and the following symbols are defined:

R radius of initial Al_8Mn_5 particle. Once some $Al_{11}Mn_4$ is present, this is the radius after correcting for the expansion of transformation.

z the ratio of the volume of product to the volume of reactant (1.47 for 4 moles of Al_8Mn_5 transforming into 5 moles of $Al_{11}Mn_4$)

α the 3D volume fraction transformed as a fraction of the original Al_8Mn_5.

The volume of the original Al_8Mn_5 particle: $\frac{4}{3}\pi R^3$

The volume of the Al_8Mn_5 core is: $\frac{4}{3}\pi r^3$

The volume of the $Al_{11}Mn_4$ shell is: $\frac{4}{3}\pi L^3 - \frac{4}{3}\pi r^3$

The volumetric expansion: $z = \frac{V_{Al11Mn4}}{V_{transformed}} = 1.47$

The volume of the transformed Al_8Mn_5 is: $\left(\frac{4}{3}\pi L^3 - \frac{4}{3}\pi r^3\right) * \frac{1}{z}$

The volume of the original Al_8Mn_5 particle = The volume of the transformed Al_8Mn_5 + The volume of the Al_8Mn_5 core.

$$\frac{4}{3}\pi R^3 = \left(\frac{4}{3}\pi L^3 - \frac{4}{3}\pi r^3\right) * \frac{1}{z} + \frac{4}{3}\pi r^3$$

$$R^3 = \left(L^3 - r^3\right) * \frac{1}{z} + r^3$$

$$R^3 = \frac{1}{z} * L^3 + r^3\left(1 - \frac{1}{z}\right)$$

$$R = \sqrt[3]{\frac{1}{z} * L^3 + r^3\left(1 - \frac{1}{z}\right)} \quad \text{Eq. 10}$$

Then using:

$$V_{remaining}^{fraction} = \frac{r^3}{R^3} = \frac{r^3}{\frac{1}{z}*L^3+r^3\left(1-\frac{1}{z}\right)} = \frac{1}{\frac{1}{z}*\frac{L^3}{r^3}+(1-\frac{1}{z})} = \frac{1}{\frac{1}{z*V_V}+(1-\frac{1}{z})} \quad \text{Eq. 11}$$

$$V_{transformed}^{fraction} = \alpha = 1 - \frac{1}{\frac{1}{z*V_V}+\left(1-\frac{1}{z}\right)} \quad \text{Eq. 12}$$

Rearranging Eq. 12,

$$\frac{1}{z*V_V} = \frac{1}{1-\alpha} + \frac{1}{z} - 1 = \frac{1-\alpha+z\alpha}{z(1-\alpha)}$$

$$V_V = \frac{1-\alpha}{1-\alpha+z\alpha} \quad \text{Eq. 13}$$

Substituting Eq. 13 to Eq. 9,

$$\overline{A_A} = 1 - \left\{\left(\frac{1-\alpha}{1-\alpha+z\alpha}\right)^{\frac{1}{3}} - \frac{1-\left(\frac{1-\alpha}{1-\alpha+z\alpha}\right)^{\frac{2}{3}}}{2} \ln \frac{1+\left(\frac{1-\alpha}{1-\alpha+z\alpha}\right)^{\frac{1}{3}}}{1-\left(\frac{1-\alpha}{1-\alpha+z\alpha}\right)^{\frac{1}{3}}}\right\} \quad \text{Eq. 14}$$

References

[1] Coleman R et al, **Can. J. Stat.** 1989, 17: 27–39.